Upscaling Calcium Carbonate Precipitation Rates from Pore to Continuum Scale

Catherine Noiriel [1,2], Carl I. Steefel [2,*], Li Yang [2] , Jonathan Ajo-Franklin [2]

[1] Géosciences Environnement Toulouse, UMR 5533 Université Paul Sabatier/CNRS/IRD/CNES, 31400 Toulouse, France

[2] Earth Sciences Division, Lawrence Berkeley National Laboratory, Berkeley, CA 94720

Catherine Noiriel

Géosciences Environnement Toulouse

UMR 5533 Université Paul Sabatier/CNRS/IRD/CNES

14, avenue Edouard Belin

31400 Toulouse, France catherine.noiriel@get.obs-mip.fr (Tel: +33 5 61 33 25 68; Fax +33 5 61 33 25 60)

Carl Steefel* (corresponding author) CISteefel@lbl.gov

Li Yang lyang@lbl.gov

Jonathan Ajo-Franklin JBAjo-Franklin@lbl.gov

Earth Sciences Division

Lawrence Berkeley National Laboratory

1 Cyclotron Road, Mail Stop 90-1116, Berkeley, CA 94720.

Abstract

The upscaling of calcite precipitation rates in porous media from the pore (micron) to continuum (centimeter) scale is evaluated with an integrated experimental and modeling approach. Experiments using cylindrical cores packed with glass beads and calcite (Iceland spar) crystals were injected over a period of 28 days with a supersaturated mixture of $CaCl_2$ and $NaHCO_3$ to induce calcite growth. Bulk rates of precipitation based on the change in aqueous chemistry over the length of the column are compared with spatially resolved determinations of carbonate precipitation using X-ray synchrotron microtomographic imaging at the micron scale. These data are supplemented by continuously-stirred reactor experiments using the same calcite seed material so as to minimize differences in the effects of reactive site density of the seed material, and to evaluate the rate of precipitation in the absence of transport or "porous medium" effects. Calcite precipitation rates determined in the stirred flowthrough reactor in this study are considerably slower than rates determined at similar supersaturation in unseeded batch experiments by Tang et al. [2008a], although these rates are compatible with those reported in Nehrke et al. [2007] for precipitation on Iceland spar when the same normalization to reactive surface area is used. The nearly linear dependence of the rates on supersaturation cannot be attributed to a diffusion control in the case of the stirred reactors and is likely the result of multi-sourced spiral growth. Integrated precipitation rates based on column effluent chemistry from a higher supersaturation experiment are in good agreement with determinations of total carbonate precipitated based on determination of pre- and post-experiment mass in the column using X-ray microtomography. Using the rates of precipitation determined in the well-stirred flowthrough reactors, it is possible to match the spatially-resolved microtomographic and aqueous data with a coarser resolution continuum model using volume-averaged flow and reactive surface area if the generation of new reactive surface area is accounted for. A nucleation or surface roughening event, which is most pronounced within two millimeters of the column inlet where the supersaturation is highest, is recorded by both BET analysis,

which indicates an increase in specific surface area from 0.012 $m^2 \cdot g^{-1}$ to a value of 0.21 $m^2 \cdot g^{-1}$ for neo-formed calcium carbonate, and by X-ray microtomography. The best fit of the column X-ray microtomography data is provided by simulating calcite precipitation either as a single nearly linear rate for multi-sourced spiral growth, or as two parallel rates that include the spiral growth model and a 2D heterogeneous nucleation model modified by a partial diffusion control, although nucleation needs to be relatively minor on a mass basis in order to match the data. The combined experiments and modeling indicate that it is possible to develop upscaled quantitative models for porous media reactivity, but changes in such properties as the reactive surface area need to be accounted for.

Keywords

Calcite precipitation kinetics, reactive surface area, reactive transport, modeling, carbon dioxide, X-ray microtomography.

1. Introduction

One of the most significant obstacles to understanding geochemical reactivity of natural subsurface environments stems from the multitude of spatial scales that have to be considered. Geochemical reactions like mineral precipitation take place ultimately at the molecular scale, but within pores that in aggregate make up the materials we call rocks, sediments, or soils. Certainly part of the reported discrepancy between laboratory-determined rates, which are typically measured on well defined mineral-water surfaces in the absence of transport effects, and field rates is likely due to the special properties of reactive porous media. Is it possible even to use laboratory-determined rates at all at the field scale? If it is possible, what kind of volume-averaging approach is needed to relate the single mineral experiments in the laboratory to the complex porous medium environment of the subsurface? Permeability is one very important parameter that has been shown to be scale dependent (Gelhar [1986], Dagan [1988]), but similar arguments can be made for mineral reactive surface area. The difficulty in characterizing volume-

averaged parameters like reactive surface area then potentially translates to questions about the homogeneity of the reactive processes themselves. Does mineral precipitation take place uniformly within the porous medium, or do gradients in precipitation rate, and thus aqueous chemistry, develop? It is highly likely that they do, as demonstrated by such studies as those of Li et al. [2006]. Even at the single pore scale, gradients may develop under certain conditions, although Li et al. [2008] demonstrated that for typical groundwater flow rates, gradients within single pores were unlikely.

One of the most important current challenges, given the complexity and range of coupled thermal, hydrological, mechanical, and chemical processes involved, is to understand geochemical reactivity in the case of long-term sequestration of carbon dioxide (CO_2) in subsurface geological formations. Massive injection of CO_2 into subsurface reservoirs will perturb significantly the geochemical equilibrium between rock-forming minerals and formation water. Initially, the injection of CO_2 and the resulting generation of an acidic brine phase will drive mineral dissolution primarily, but with addition of alkalinity and suitable cations from the formation water and the dissolution of primarily minerals, precipitation of carbonates is expected to occur.

Several models have been proposed to describe rate of calcite precipitation based on affinity models of surface-controlled crystallization (e.g. Aagaard and Helgeson [1982]). A general equation to describe the rate of calcite precipitation is (Lasaga [1981]):

$$R_{ppt} = k\left[\exp\left(\frac{m\,\Delta G}{R^{*}\,T}\right)-1\right]^{n} = k\left[\left(\frac{IAP}{K_{sp}}\right)^{m}-1\right]^{n} = k\left(\Omega^{m}-1\right)^{n} \qquad (1)$$

with k the rate constant (mol·m^{-2}·s^{-1}), ΔG the Gibbs free energy change of the overall reaction (J·mol^{-1}), Ω the saturation index ($\Omega = IAP / K_{sp}$), K_{sp} the solubility of calcite, IAP the ion activity product defined by $IAP = a_{Ca^{2+}} a_{CO_3^{2-}}$, with $a_{Ca^{2+}}$ and $a_{CO_3^{2-}}$ the activities of Ca^{2+} and CO_3^{2-}, respectively, R^{*} the gas constant (J·K^{-1}·mol^{-1}) and T the absolute temperature (K). The value of n and m are semi-empirical constants that depend on the kinetic behavior involved in the chemical reaction, although m can be

interpreted as the Temkin coefficient relating the reaction stoichiometry in the rate limiting step to the reaction stoichiometry of the overall reaction (Aagaard and Helgeson [1982], Oelkers et al. [1994], Tang et al. [2008a]). For example, a value of $n = 1$ (linear rate law) has been attributed to crystallization limited by adsorption of lattice ion (Nielsen [1984]), although it may also be ascribed to a rate controlled by diffusion (e.g., Pokrovsky et al. [2005]) and in some cases to a multi-source spiral growth mechanism (Teng et al. [2000]). A second order equation ($n = 2$) may be used to describe growth at single screw dislocation by the spiral mechanism (Teng et al. [2000]), while high order dependences ($n > 2$) can be applied to growth both at screw and edge dislocation (Blum and Lasaga [1987]) or growth by 2D nucleation (Teng et al. [2000]). For example, Teng et al. [2000] observed on AFM images a transition from spiral growth mechanism (observed at $\log \Omega = 0.17$) to two-dimensional surface nucleation (observed at $\log \Omega = 0.43$ and $\log \Omega = 0.69$). Despite the different expressions that have been proposed, these formulations share the concept of linking growth mechanisms to the saturation index ($\log \Omega$), although Teng et al. [2000] provide a thoughtful commentary on the difficulties associated with linking the reaction order uniquely to a single mechanism.

Carbonate precipitation is important not only because it represents an important sequestration mechanism for CO_2, but also because it can modify the physical and chemical properties of the subsurface medium. Pore clogging and the resulting reservoir injectivity decrease is certainly one such process that can take place, but changes in reactivity are also possible as either primary minerals are passivated due to coatings, or reactivity is enhanced as a result of the growth of new, high specific surface area reactive material. In addition, the newly precipitated material may have a higher reactive site density than was present on the original seed material. These effects, however, are presently poorly understood because of the lack of detailed investigations at the pore scale.

One possible approach to understanding the role of multi-scale processes in a complex enterprise like subsurface CO_2 injection, and perhaps even to address the lab-field rate discrepancy (White and Brantley [2003]), is to investigate rates in an ideal system where physical and chemical heterogeneities, if present,

are minor (Steefel et al. [2005]). In this study, we began with continuously-stirred reactor experiments using coarsely crystalline calcite (Iceland spar) to determine the rate of precipitation for this particular material as a function of supersaturation. A thorough study of calcite precipitation kinetics is not within the scope of this study, but it will likely be important to know the intrinsic reactivity of the material as compared to other possible calcite seeds that may have a different reactive site density. As an ideal representation of a porous medium, a column filled with a mixture of glass beads and Iceland spar grains was packed and injected with a $CaCl_2$-$NaHCO_3$ mixture that is supersaturated with respect to calcite. The bulk reactivity of grains in the column was evaluated through a combination of effluent chemistry and reactive transport modeling, and these data were compared with X-ray microtomography imaging (XMT) at the micron scale of pre- and post-experiment materials to quantify the mass of precipitate added to the column. Of particular interest is the spatial distribution of reaction products and whether these can be captured at the larger scale by a continuum model using volume-averaged rate constants.

2. Materials and methods

2.1. Starting materials

The stirred reactor experiments were carried out using crushed calcite spar crystals and the plug-flow column experiments were conducted with the same crushed calcite spar crystals mixed with glass beads. Photomicrographs of the materials are presented in Figure 1 and chemical composition is given in Table 1.

Glass beads are acid-washed soda-lime glass of density 2.5 $g{\cdot}cm^{-3}$ in the range 425-600 µm (Sigma G8772). Calcite that began as centimeter-size crystals were crushed in an agate mortar and then sieved in the range 355-500 µm. The initial specific surface area determined by multipoint krypton adsorption BET method was 0.012 $m^2.g^{-1}$. Assuming an average grain size of about 425 µm for crushed calcite grains, a spherical geometry would result in a geometric surface area of 0.005 $m^2{\cdot}g^{-1}$. The difference between the spherical geometry and the measured value of 0.012 $m^2{\cdot}g^{-1}$ indicates a correction for geometry and

roughness of approximately 2.303. An assumption of a rhombohedral geometry would yield a higher geometric estimate and therefore a value closer to the BET-determined surface area, but considering the range of grain sizes and the observations with SEM of surface roughness, we use the factor of 2.303 based on an ideal spherical geometry. All the materials were washed with deionized water, put into an ultrasonic bath to clean the surface and eliminate fine particles, and then dried in an oven at 50°C for several hours before being used in the experimental studies.

2.2. Experimental procedure

2.2.1. Continuously-stirred precipitation rate experiments

So as to provide a base case for the plug-flow column experiments, flow through experiments seeded with the ground and sieved calcite spar crystals were conducted in continuously stirred reactors (CSTR) to determine the rate of calcite precipitation under chemical conditions similar to those of the plug-flow columns experiments, i.e. with a saturation index (log Ω) ranging from about 0.15 to 0.82.

The stirred reactor experiments were carried out in 70 ml reactors at a total flow of 0.5 $ml \cdot h^{-1}$, with separate streams of $NaHCO_3$ and $CaCl_2$ stock solutions pre-equilibrated with atmosphere and mixed directly in the reactor through two separate injection ports. The chemistry of the mixed injection solution was determined by collecting both streams in a sampling vessel while maintaining the same pump speed. The reactors have a suspended Teflon-coated stirring rod operated at a constant stirring rate of 800 RPM. Each of the experiments used an initial mass of calcite spar, m_{init}, of 1 g as seed crystals.

The specific surface area of newly crystallized calcium carbonate was determined by measuring the initial and final specific surface areas using a five point krypton gas BET method, with weighting based on the relative masses of initial and new precipitate according to:

$$SSA_{fin} = \frac{m_{init}}{m_{ppt} + m_{init}} SSA_{in} + \frac{m_{ppt}}{m_{ppt} + m_{init}} SSA_{ppt} \qquad (2)$$

where SSA_{in} and SSA_{fin} are the initial and final specific surface areas determined with the BET method and SSA_{ppt} is the specific surface area of the new precipitate calculated from Eq. 2 using the m_{init} and m_{ppt}, the initial and newly precipitated calcite mass, respectively (Table 2). This approach does not take into account the details of the reactive site density and coverage of the surface, nor does it account for the fact that epitaxial growth will likely generate little new surface area (this is discussed below in the context of 2D nucleation versus epitaxial growth). Thus, it simply represents an average of the surface area associated with newly formed calcite.

Calcium and sodium were determined in the injection solution and effluent by ICP-MS analysis after acidification with nitric acid (pH < 2). pH was determined with an Orion pH electrode. Dissolved Inorganic Carbon (DIC) was assumed to equal the sodium concentration in the injection solution, which was prepared using reagent grade $NaHCO_3$. In the effluent, DIC was estimated by assuming that the stirred reactors behaved as closed systems in which calcium carbonate was the only phase precipitated such that $\Delta Ca = \Delta DIC$ (Table 2). Saturation indexes for the well-mixed effluent were calculated with the code CrunchFlow, which makes use of the EQ3 database (Wolery et al. [1990]). Activity coefficients are calculated with the extended Debye-Hückel equation. Thermodynamic parameters at 22°C are included in Table 3.

Precipitation rates, R ($mol \cdot m^{-2} \cdot s^{-1}$), are determined by the difference between the concentration of calcium determined in the effluent, Ca_{out}, and the well-mixed stock solution, Ca_{in} according to:

$$R = -Q \frac{Ca_{out} - Ca_{in}}{A} \qquad (3)$$

where Q is the volumetric flow rate ($l \cdot s^{-1}$), and A is the total surface area (m^2) in the reactor at steady state calculated using the final mass of calcium carbonate and specific surface area in the reactor based on BET measurement.

2.2.2. Plug-flow column precipitation experiments

Three samples (REAC-0 to REAC-2) were prepared by packing different amounts of glass beads with or without calcite crystals in cylindrical plug-flow column reactors of 6.50 mm diameter and of approximately 12 mm length. The relative proportions of calcite spar and glass beads used in each of the experiments are given in Table 4.

The inlet fluid used in the experiment was a 50-50 % mixture of $CaCl_2$ and $NaHCO_3$ stock solutions prepared from reagent-grade salts dissolved in deionized water. The composition of the inlet solution for each reactor is given in Table 5. They correspond to a calcite saturation index, log Ω, of either 0.70 or 1.42. Each reactor was injected with the stock solutions pre-equilibrated with atmosphere using a multi-channel syringe pump at a controlled flow rate of 0.25 $cm^3.h^{-1}$ for each channel ($Q = 6.94\ 10^{-8}\ l{\cdot}s^{-1}$), and mixed through a T-valve at approximately 6 cm from the reactor inlet, as shown schematically in Figure 2. Consequently, the flow rate within the plug-flow reactor was 0.5 $cm^3.h^{-1}$ ($Q = 1.38\ 10^{-7}\ l{\cdot}s^{-1}$).

The combined calcite spar and glass beads resulted in a porosity of approximately 37 % in the packed columns based on microtomographic and gravimetric determinations. The residence time of fluid in the plug-flow column was approximately 20 min, while the residence time in the pre-mixing chamber was approximately 5.5 min. The experiments were conducted for 28 days at room temperature (22°C). Before the experiments, the samples were saturated with water under vacuum and injected with an acidic solution (deionised water + 0.001 M HCl, pH 4.01) at a flow rate of 20 $ml.h^{-1}$ ($Q = 5.56\ 10^{-9}\ m^3{\cdot}s^{-1}$) for 5 h to further clean the mineral surfaces and eliminate fine particles.

The pH of both the inlet and outlet solutions was measured using an Orion pH electrode. In addition, major and minor elements were measured in solution by inductively coupled plasma mass spectroscopy (ICP-MS), after acidification with nitric acid (pH < 2). Aliquots of inlet and outlet solutions were also sampled with a capped vial under an N_2 atmosphere to analyze the total inorganic carbonate content using a total inorganic carbon analyzer (TIC).

3. Characterization and analytical procedure regarding plug-flow experiments

3.1. Analysis of 3D geometry of plug-flow columns with X-ray microtomography

The geometries of the three packed columns REAC-0 to REAC-2 were characterized by X-ray microtomography (XMT) at Beamline 8.3.2 at the Advanced Light Source of Lawrence Berkeley National Laboratory. The XMT method is based on a 3D reconstruction from a thousand 2D radiographs of the X-ray attenuation properties of the various materials forming the columns. As air, glass beads and carbonate minerals in the column reactors have different chemical compositions and densities, their attenuation properties are different. Therefore, they can be differentiated on the 3D images.

The optical system used in the experiment provides a spatial resolution of 4.46 µm (pixel size). Two data sets were collected, before (time t_0) and after (t_1) the experiment. As the camera field is shorter than the height of the sample, several scans were set up vertically and data were stitched together after reconstruction. Tomographic reconstruction was done with the software package Octopus (Dierick et al. [2004]) through use of the filtered back-projection algorithm. The reconstruction provides 3D images of the X-ray absorption by the different materials in the sample. Each data set is 1600 × 1600 × 3000 voxels. A voxel is defined as a pixel cubed and is represented as a volume of 4.46 × 4.46 × 4.46 μm^3.

Image processing was carried out using the Avizo® software. By using an appropriate image processing procedure, it is possible to distinguish the different materials (e.g air, glass beads, and calcite) and accurately quantify parameters characterizing the sample geometry, i.e. porosity distribution, pore connectivity as well as geometric surface-area of the fluid-rock interface (Noiriel et al. [2004], Noiriel et al. [2005]). Each of these parameters is based on averaging of a single 4.46 micron slice through the column. To do this, the images were segmented; that is, the voxels belonging to the pore space were distinguished from those belonging to the solid matrix. As data are noisy and present phase contrast, a segmentation technique based on threshold values coupled with erosion-dilatation procedure was chosen to separate the different materials (Gonzales and Woods [1992]). Before the segmentation procedure, the

data sets were normalized through a linear interpolation procedure to achieve consistency within a dynamic range of intensity values on the different images. The images were registered and the noise was reduced by running a 3D median filter. Then, the different parameters for segmentation were chosen by visual inspection of the grey-level histogram and of the segmented volumes by comparison with the grey-scale ones. At the end of the procedure, the pore space was separated from calcite and glass beads (Figure 3).

3.2. Quantitative determination of the extent of the reaction

The mass of calcite precipitated in the columns was determined by two different but complementary methods, i) chemical analysis of the effluent, and ii) XMT. The methods give complementary information at two different scales, the first recording the spatially integrated rate over the 12 mm length of the column, the second recording the time integrated rate within a single 4.46 μm slice through the column.

The volume of precipitated calcite as the porosity changes were estimated from the difference in Ca concentration between the sample inlet and outlet. Because only calcite has precipitated during the experiments (see discussion below), the volume of precipitated calcite at time t_i is given by:

$$V_{cal}(t_i) = Q \times \upsilon_{cal} \int_{t=t_o}^{t=t_i} \Delta\text{Ca}\, dt \qquad (4)$$

with V_{cal} the volume of calcite precipitated , Q the volumetric flow rate ($m^3 \cdot s^{-1}$), υ_{cal} the molar volume of calcite ($m^3 \cdot mol^{-1}$), and ΔCa the change in calcium concentration between the inlet and the outlet of the sample ($mol \cdot m^{-3}$). The spatially integrated porosity over the length of the columns at time t_i is given by:

$$\phi_{Ca}(t_i) = \phi_0 + \left(Q \times \upsilon_{cal} / V_T\right) \int_{t=t_o}^{t=t_i} \Delta\text{Ca}\, dt \qquad (5)$$

where ϕ_{Ca} is the porosity calculated from the change in Ca concentration across the column, and ϕ_0 is the initial sample porosity (at t_0). This calculation is essentially the same as the one used to determine the net

reaction in the stirred reactor experiments described above, but with conversion from moles to volume using the molar volume value for calcite.

In samples REAC-0 and REAC-2, the volume of calcite precipitated was not sufficient to characterize with XMT. In contrast to these columns, the amount of calcite precipitated in column REAC-1 was significant enough to be followed and characterized using XMT. After segmentation of the XMT images, the total porosity of the sample ϕ is simply the ratio of the pore space to the total volume of the sample V_T. The local porosity $\phi(z)$ can also be calculated for each slice along the flow axis. It is also possible to calculate the volume of precipitated calcite by calculating the difference in the number of calcite voxels (or solid pixels) observed at the end (t_1) and the beginning (t_0) of the experiment:

$$V_{cal}^{'} = \sum_{V_T} \left(N_{cal}(t_1) - N_{cal}(t_0) \right) \times V_{pix} \qquad (6)$$

with N_{cal} the number of calcite voxels in the image, the total volume of the sample, and V_{pix} the volume of a voxel (V_{pix} = 4.46×4.46×4.46 µm^3). The surface-area (m^2) of the calcite crystals is defined as the number of fluid-calcite edge voxels $N_{cal\text{-}fluid}$ multiplied by the voxel surface-area (S_{pix} = 4.46×4.46 µm^2). The geometric surface-area normalized to the mass of calcite, $S_{geo}^{'}$ (m^2·g^{-1}), is defined by:

$$S_{geo}^{'} = \sum_{V_T} N_{cal-fluid} \times S_{pix} / \rho_{cal} \times V_{cal}^{'} \qquad (7)$$

with ρ_{cal} the density of calcite.

3.3. Reactive transport modeling

Reactive transport modeling using the code CrunchFlow was used to interpret both the voxel-scale microtomography results and the effluent chemistry from the plug-flow column. The code CrunchFlow, or its predecessors, has been used for over 20 years to simulate mineral precipitation (and dissolution) in porous media (Steefel and Van Cappellen [1990], Steefel and Lasaga [1990], Steefel and Lasaga [1994], Steefel and Lichtner [1994], Maher et al. [2009]). The software solves a set of partial differential

equations for the conservation of aqueous and solid mass, with treatment of fluid flow, molecular diffusion, and multicomponent reaction at the continuum scale:

$$\frac{\partial}{\partial t}\left(\phi C_i\right) + \nabla \bullet \left(-\mathbf{D}\nabla(C_i) + qC_i\right) = -\sum_m \nu_{im} R_m \tag{8}$$

where **D** is the dispersion tensor, including both kinematic dispersion and molecular diffusion, C is the concentration, q is the Darcy flux, R_m is the rate of reaction (precipitation or dissolution) of the mineral m, and ν_{im} is the stoichiometric coefficient that gives the number of moles of component i in mineral m. For a given mineral, multiple kinetic pathways can be considered that operate simultaneously:

$$R_m = \sum_p R_p \tag{9}$$

where R_p is a parallel kinetic pathway. An example is the simultaneous inclusion of a 2D heterogeneous nucleation pathway operating at the same time as a spiral growth precipitation mechanism, as considered in this work. The principle application of the code CrunchFlow is to the upscaled continuum problem, which uses volume averaged values of the porosity and reactive surface area. While the porosity change associated with mineral precipitation is expected to modify the permeability as well, methods to measure the pressure gradient over the length of the short column were not available at the time of the experiment. Therefore, it is assumed that permeability remains constant over the time scale of the experiment in the modeling. Measurements of effluent fluid mass verify that the overall flow rate remained relatively constant using the syringe pumps.

For initial conditions, the mass of calcite added to the columns was assumed to be spread evenly over the length of the column, resulting in an average volume fraction of calcite spar of 20 %. To estimate the initial reactive surface area, we used the value of 0.012 $m^2 \cdot g^{-1}$ determined by BET method. However, any new calcium carbonate formed was assumed to have a specific surface area of 0.21 $m^2 \cdot g^{-1}$ based on the discussion below. The effect of using various rate laws and specific surface areas to match the observed

distribution of reaction products in the columns can then be evaluated with the reactive transport modeling.

An advection-dominated flux based on the measured flow rate was used as an upstream Neumann boundary condition for the plug-flow column experiments. The chemistry of the injection solution is described in Table 5.

The 12 mm length of the column is discretized using a constant grid spacing of 0.1 mm, with the exception of a single grid cell of 3.645 mm corresponding to the mixing manifold at the inlet of the column. The grid cell corresponding to the mixing manifold is intended to match the approximately 5.5 minute residence time of solution in this chamber just upstream from the packed column itself.

A detailed pore scale simulation of the plug-flow column is currently beyond the capabilities of CrunchFlow, although we do present the results of calculations that resolve 10-30 μm diffusion boundary layers next to reacting calcite grains so as to evaluate the potential for a diffusion control (partial or complete) on precipitation rates. For these calculations, a Dirichlet (fixed concentration) boundary condition is used at either 10 or 30 μm from the calcite surface. The 10 and 30 μm boundary layers were considered based on the discussions presented in Hintz and Johnson [1989] and Sugano [2008] working in the field of pharmaceutics. Hintz and Johnson [1989] presented a model for the width of the diffusion boundary layer in the case of a dispersion of grains within a stirred fluid medium. Their analysis, which was based on calibration to measured dissolution rates, determined an empirical maximum width of 30 μm for the boundary layer as grain size increased. Sugano [2008] arrived at similar conclusions, but made use of a Fluid Dynamic (FD) model to incorporate more rigorously the effects of both stirring rate and grain size. Sugano [2008] showed that the width of the diffusion boundary layer, h_{eff}, affects the diffusion-controlled flux to the mineral surface according to:

$$\frac{\partial C}{\partial t} = A \cdot D_{eff} \frac{1}{h_{eff}} \left(C_s - C_B \right) \qquad (10)$$

where A is the mineral surface area, D_{eff} is the effective diffusion coefficient, C_s is the concentration in the aqueous phase immediately adjacent to the mineral surface, and C_B is the concentration of the reacting species in the bulk solution. In a strictly diffusion controlled regime, C_s would be the solubility, but a more general treatment is considered here in which C_s is computed based on dynamics of the boundary layer given appropriate boundary conditions for the bulk solution, reaction rate at the mineral surface, and diffusion rates for all of the reacting species. In other words, the full reactive transport equation (Eq. 8), with coupling of diffusion through the boundary layer and reaction at the mineral surface, is solved in the case presented here. This allows for a partial rather than complete control by diffusion, since the actual behavior depends on the ratio of the rate constant and diffusion coefficient for a given length scale. For a spherical particle, the width of the hydrodynamic diffusion layer, h_{eff}, is given by:

$$\frac{1}{h_{eff}} = \frac{Sh}{2r_p} \tag{11}$$

where Sh is the Sherwood number and r_p is the particle radius (Sugano [2008]). The Sherwood number can be related to the Reynolds number:

$$\mathrm{Re}_p = \frac{2r_p \mathrm{v}_{rel,tot}}{\nu} \tag{12}$$

where $\mathrm{v}_{rel,tot}$ is the total relative velocity of the particle against the fluid flow and ν is the kinematic viscosity, and the Schmidt number:

$$Sc = \frac{\nu}{D_{eff}}. \tag{13}$$

The Sherwood number can be estimated from the semi-empirical Ranz-Marshall correlation often used for a spherical particle (Ranz and Marshall [1952]):

$$Sh = 2 + 0.6\,\mathrm{Re}_p^{1/2}\,Sc^{1/3}. \tag{14}$$

Based on this FD model, Sugano [2008] was able to estimate a hydrodynamic diffusion layer of about 30 μm for large grains (250 μm radius) under largely stagnant conditions, in agreement with Hintz and Johnson [1989]. For a stirred solution, Sugano [2008] estimated a hydrodynamic diffusion layer thickness of approximately 10 μm. These values then were used to bracket the diffusion boundary layer calculations carried out with CrunchFlow.

The diffusion boundary layer calculations are carried out with a constant grid spacing of 100 nanometers (0.1 μm), resulting in a total of either 100 or 300 grid cells depending on whether the 10 or 30 μm boundary layer was considered. For surface area in Eq. 10, we used the geometric surface area for a 420 μm diameter calcite grain (in the middle of the range of the sieved grain size), with an additional surface roughness factor of 2.303 based on BET measurements of the initial calcite spar crystals. In the CrunchFlow calculations, all of the reacting surface area is considered to be present within a single spherical geometry grid cell of 0.1 μm thickness, as in the calculations presented in Li et al. [2008]. The rest of the domain is solution only and mineral precipitation is not allowed. In practice, the calculation using CrunchFlow requires that a geometric surface area (with the addition of a surface roughness factor, where appropriate) relative to the grid spacing is provided. For the 0.1 μm grid cell with a volume of 4.02×10^{-5} cm^3, the geometric surface area of a 210 μm radius perfectly spherical grain is given by 10^7 $m^2\cdot m^{-3}$. Adding the surface roughness factor indicated by the difference between the BET-determined value for the specific surface area and the ideal geometric estimate (see above), we arrive at a numerical grid-size dependent (0.1 μm spacing) value for the surface area immediately adjacent to the calcite grain of 2.304×10^7 $m^2\cdot m^{-3}$. Diffusion coefficients used in the calculation are given in Table 6. The multicomponent diffusion equation based on the Nernst-Planck equation is solved, which preserves electroneutrality while allowing for the different diffusion rates of the ions (Giambalvo et al. [2002], Steefel and Maher [2009]).

4. Results

4.1. Rates of calcite precipitation in CSTR experiments

Rates of calcium carbonate precipitation determined from the Continuously Stirred Reactor (CSTR) experiments, and normalized to the physical surface area of calcite measured by BET measurement at the end of the experiment, are summarized in Table 2. The rates are plotted as a function of the saturation index (log Ω) in the reactor in Figure 4 and can be described by the expression:

$$R = 1.79 \pm 0.28 \times 10^{-9} \left[\exp\left(\Delta G / R^{*} T \right) - 1 \right]^{1.12 \pm 0.1} \qquad (15)$$

As discussed previously, the BET measurements of calcite physical surface area in the CSTR experiments were used to estimate an average specific surface area based on the mass weighted average of the BET surface area before and after the experiment. Final BET surface areas for experiments CS-1, CS-2, CS-3, and CS-4 were 0.013, 0.015, 0.013, and 0.016 $m^2 \cdot g^{-1}$, respectively (each with a 10 % uncertainty in their value). These determinations lead to an estimate of the specific surface area of 0.21 $m^2 \cdot g^{-1}$ for calcium carbonate precipitated during the experiment, a value that is compatible with that determined by Tang et al. [2008a] of 0.26 $m^2 \cdot g^{-1}$ at the end of their experiments.

4.2. Solution chemistry from plug-flow column reactors

The chemical compositions of the inlet and outlet solutions show a decrease of calcium concentration over the length of the column (ΔCa>0) as a result of calcite precipitation (Figure 5). Decrease is on average higher for REAC-1 (ΔCa = 4.0 10^{-4} M) compared to REAC-2 (ΔCa= 4.0 10^{-5} M). The temporal evolution of the concentrations in the solutions during the precipitation experiments is presented in Figure 5. Calcium concentration is almost constant with time, even if the outlet solution concentrations present a slight decrease with time for REAC-2. For REAC-1, fluctuations are attributed to slight changes of the flow rate of the pumps as Ca concentration is anti-correlated with Na concentration, which is used as a monitor of the mixing efficiency since it is conservative. The pH also slightly decreases during

experiments. The outlet solutions remain highly oversaturated with respect to calcite; the saturation index of the outlet solution log Ω drops to 1.17 for REAC-1, and remains close to 0.70 for REAC-2.

4.3. Determination of mineralogy of reaction products

Raman spectroscopy was used to determine the identity of the calcium carbonate precipitates from the plug-flow column. Raman spectra were recorded with a LabRam HR800 Jobin-Yvon™ microspectrometer using 532 nm (green) laser excitation. The data indicated a good match with calcite (as identified by its four absorption bands at 1088 (ν1-symmetric CO_3 stretching), 714 (ν4-symmetric CO_3 deformation), 284 and 157 (Ca and CO_3 bond vibration) cm^{-1}), although purely based on this data, the initial formation of vaterite, which has a solubility about 0.58 log Ω units above that of calcite (De Visscher and Vanderdeelen [2003]), cannot be ruled out, since vaterite typically transforms to calcite over relatively short time scales. It should be pointed out, however, that that the precipitation rates determined in the well-stirred reactors (Figure 4) appear to be completely continuous across what would be the solubility limit of vaterite. It is highly unlikely that the curve for the rate would be continuous if two distinct reactive phases were involved.

4.4. Calcite nucleation and growth

The volume of precipitated calcite V_{cal} over the length of the plug-flow columns calculated from the effluent chemistry is 4.94 and 0.57 mm^3 for REAC-1 and REAC-2, respectively. The value for REAC-1 is very close to the volume obtained by XMT (V'_{cal} = 5.03 mm^3 for an initial amount of calcite in the sample equal to 63.86 mm^3), which demonstrates the ability of XMT to accurately measure changes in calcite content given enough accumulation of precipitate.

Observations of the samples from REAC-1 and REAC-2 after the conclusion of the experiments indicate differences both in the crystal growth rate, amount and morphology that appear to depend on two main factors: the initial surface for calcite growth (i.e. glass bead or calcite spar) and the saturation index

log Ω. The growth rates were highest close to the column inlets where the supersaturation was highest, as evidenced by the volume % of calcite precipitated (Figure 6). In particular, the first mm of column REAC-1 shows porosity decrease of up to 6.8 %. As the saturation index decreases, either between samples REAC-1 or REAC-2, or between inlet and outlet of sample REAC-1, the number of calcite crystals formed on glass bead surfaces decreases. This is also an expected outcome to the extent that the solution supersaturation falls below the 2D nucleation threshold (Teng et al. [2000]) within the column due to consumption of calcium and carbonate. In general, new calcite crystals grew preferentially on the calcite spar surfaces compared to the glass beads in the column (Figure 7a and 7b). Additional observations with SEM (Figure 8) show that the shape of new calcite crystals differs greatly according to the initial nucleation surface. The glass beads' surface displays small, individual rhombohedral crystals (i.e. without any link to the spar surface). Conversely, the growth of calcium carbonate on spar is epitaxial, i.e. oriented on the single spar surfaces. Some 2D heterogeneous nuclei are visible as well.

By subtracting registered 3D volumes (Figure 7c), it is possible to follow the shift of the fluid-rock interface during the experiment. Figure 7c shows that the size of the crystals on glass beads or the thickness of the new precipitated calcite layer on spar are variable, indicating a spatial variability of the growth rates within the pores and/or different stages of calcite nucleation and growth. It is worth noting that precipitation of calcite was detected across the length of the plug-flow column on spar surfaces, whereas there is little evidence of precipitation on glass beads at distances greater than about 1-2 mm from the sample inlet.

4.5. Surface area changes

Calcite growth resulted in an increase of the surface roughness of both the glass beads and original spar crystals (Figure 9). As a consequence, measurement of the geometric surface area and specific surface with XMT reveals an increase of the fluid-calcite interface area with time for REAC-1 over approximately the first 0.75 mm of the column length (Figure 10). Over this interval, the specific surface area increases from a value of about 0.0075 ± 0.0002 $m^2 \cdot g^{-1}$ to an average value of approximately 0.024

$m^2 \cdot g^{-1}$, but locally with values as high as 0.058 $m^2 \cdot g^{-1}$. The measurement of the specific surface area using this approach is limited by the resolution of the XMT technique, which cannot measure sub-micron features given the voxel size of 4.46 μm, but the observations are compatible with others based on the SEM images and the BET determinations. The background value of 0.0075 $m^2 \cdot g^{-1}$ agrees fairly well with the estimate of 0.005 $m^2 \cdot g^{-1}$ based on average grain size (425 μm) and an ideal spherical geometry. The values for specific surface area over the first 0.75 mm of the column are actually higher than those determined in the stirred cell experiments, suggesting a more prominent role for 2D heterogeneous nucleation in the higher supersaturation columns. The value for the specific surface area of 0.21 $m^2 \cdot g^{-1}$ for the neo-formed calcium carbonate estimated from the BET analysis is higher, but this represents only the calcium carbonate precipitates, not the combination of precipitates and original calcite spar. Nonetheless, the XMT mapping of specific surface area makes it clear that a distinct surface roughening event that coincides with the greatest addition of calcium carbonate mass occurs over the first part of the column where the supersaturation is highest.

5. Discussion

5.1. Interpretation of rates from stirred reactors

The primary objective of the stirred reactor experiments was to provide a baseline rate of calcium carbonate precipitation as a function of saturation state (log Ω) on the calcite spar seeds in the absence of "porous medium" effects. As Teng et al. [2000] made clear in their analysis of how the velocity of individual steps on the calcite surface relate to the overall supersaturation (and thus, to the applicability of overall "affinity-based" rate laws), the bulk rate depends on the range of mechanisms that are operative, as well as the density of individual reactive sites. This implies that not all materials may show the same bulk rates of precipitation given the potentially very different reactive site distributions per unit surface area of calcite. In addition, there may be issues even in the case of well-mixed stirred reactors to the extent that a diffusion boundary layer develops, since Pokrovsky et al. [2005] have shown that a diffusion

control (or partial control) is possible for dissolution of calcite even at circumneutral pH. A partial diffusion control is also possible in a more nearly stagnant column experiment (no stirring), or in the case where the grains are large, as suggested by the analysis of Sugano [1998].

Figure 11 compares the rates of precipitation determined in this study with those determined by Tang et al. [2008a,b] at 25°C at similar supersaturation. Rates determined by Tang et al. [2008a] are close to an order of magnitude more rapid those measured in this study. Some of this may be related to the experimental approach outlined in Tang et al. [2008b] and used in Tang et al. [2008a], which made use of pH-stat batch reactors without seeds to determine the rate. In their study, one can observe significant changes in precipitation rate by as much as a factor of 7 over time, as for example with their samples 20, 12, and 13, all measured at a saturation index of 1.11-1.12, but at times ranging from 9 to 14 to 59 min, respectively (Tang et al. [2008a]).

Tang et al [2008a,b] are not the only ones that report rates of precipitation higher than those observed in this study. The Shiraki and Brantley [1995] data, if extrapolated to 25°C using an activation energy of 48 $kJ \cdot mol^{-1}$ (Pokrovsky et al. [2005]), would yield a rate constant of about $10^{-6.33}$ $mol \cdot m^{-2} \cdot s^{-1}$, while the direct measurements of precipitation at 25°C by Nancollas and Reddy [1971] and Inskeep and Bloom [1985] yield rate constants of $10^{-6.86}$ and $10^{-6.41}$ $mol \cdot m^{-2} \cdot s^{-1}$, respectively. Some of these experiments were seeded, so the difference cannot be attributed completely to the presence or absence of a discrete nucleation event in the absence of seed material.

Comparing the rates of precipitation with calcite dissolution rates is more difficult, since the same mechanisms need not apply. Pokrovsky et al. [2005] determined a dissolution rate constant for calcite of $10^{-6.44}$ $mol \cdot m^{-2} \cdot s^{-1}$. In addition, Li et al. [2008] found a good match for dissolution of the same calcite spar used in this study in a single pore using the rate law proposed by Chou et al. [1989], which contains a pH independent term of $10^{-6.18}$ $mol \cdot m^{-2} \cdot s^{-1}$. More recently, Hassenkam et al. [2011] found a rate of dissolution of Iceland spar calcite of $10^{-5.28}$ $mol \cdot m^{-2} \cdot s^{-1}$.

Another potential clue for the difference in results is suggested by the higher order dependence of the calcium carbonate precipitation rate on ΔG observed in the Tang et al [2008a,b] experiments. At higher temperature and/or supersaturation, 2D heterogeneous nucleation may be the dominant growth mechanism. Teng et al. [2000] reported that at log Ω of about 0.7, 2D heterogeneous nucleation dominated, while at superaturation as low as log Ω = 0.34, spiral growth and 2D heterogeneous nucleation may coexist. Without seeds in the Tang et al [2008a,b] experiments, nucleation was the only means by which calcite could be precipitated initially and evidently their data record such discrete nucleation events. This conclusion is further reinforced by the higher order dependence of the Tang data on supersaturation, with a best fit given using an exponent n = 3.2 as fitted in this study using only 25°C data from Tang et al. [2008a]. The data in this study, in contrast, show a best fit over the range of saturation states considered with n = 1.12 (Eq. 15). These compare with an exponent of 1.16 determined by Nancollas and Reddy [1971] at 25 °C and 1.09 by Shiraki and Brantley [1995] for some of their vigorously stirred batch experiments carried out at intermediate supersaturation at 100°C. Shiraki and Brantley [1995] attributed their linear data to a rate control by adsorption, but it seems more probable that in the experiments described in this study, a multi-sourced multiple spiral growth mechanism is operative (Teng et al. [2000]). Teng et al. [2000] show that the rate of a multi-sourced, multiple spiral growth mechanism is given by:

$$R_m = \frac{a_e \omega \beta m' k_B T\left(\Delta G / R^* T\right)}{8\omega\alpha + 2\Lambda k_B T\left(\Delta G / R^* T\right)}\left[\exp\left(\Delta G / R^* T\right) - 1\right] \qquad \textbf{(16)}$$

where a_e is is the equilibrium activity of the solute, β is the rate constant (in units of length over time), ω is the molar volume of the mineral, k_B is the Boltzmann constant, T the absolute temperature, α is the step edge free energy (per unit length per unit height), m' is the number of screw locations and Λ is the length of the line over which these m' screw locations occur. In cases where the second term in the denominator of Eq. 16 dominates over the first, as in the case of surface imperfections, the ΔG terms in the numerator and denominator may cancel, resulting in a linear or nearly linear dependence on ΔG (Teng et al. [2000]).

Another possible source of the discrepancy between the experiments reported here and those in other studies may relate to a partial or complete control of the rate by molecular diffusion. The observation by Pokrovsky et al. [2005] that a partial diffusion control occurred even at circumneutral pH was based on the observed stirring rate dependence of the dissolution rate. Whether a partial or complete control by diffusion occurs depends on the relative rates of surface reaction versus diffusion. This effect can be investigated using numerical modeling if the size of the diffusion boundary layer, designated as h_{eff} above, can be estimated. Under stagnant conditions and a grain size averaging about 420 μm, the analysis of Hintz and Johnson [1989] and Sugano [2008] suggest a diffusion boundary layer of about 30 μm. If we assume that the rates determined by Tang et al. [2008a] are surface reaction-controlled rates, which seems reasonable given the stirring of their solutions and the small grain size (the width of the hydrodynamic boundary layer scales with the grain size and approaches the asymptotic molecular diffusion limit for crystals less than about 10 μm), we can calculate the rates for the large crystals used in this study assuming some potential mixture of surface reaction and diffusion control. This is done by solving for the surface reaction rate at the mineral surface using the Tang et al. [2008a] rates simultaneously with multicomponent diffusion across the width of the hydrodynamic diffusion layer, h_{eff}. The 30 μm boundary layer calculations can also be compared with the 10 μm boundary layer case, which is more likely for the well-stirred reactors. Figure 12 shows the saturation state (log Ω) in the boundary layer calculated as a function of distance from the crystal surface for these two cases. In each case, the surface reaction rate in the single grid cell containing the reactive calcite is taken from the study of Tang using a rate law of the form:

$$R = 1.40 \times 10^{-9} \left[\exp\left(\Delta G / R^{*} T \right) - 1 \right]^{3.2} \qquad (17)$$

which is based on the fit of the Tang et al. [2008a] data shown in Figure 11. The high rate of precipitation at 25°C predicted by the Tang data, and as captured by Eq. 17, results in a flux at the mineral surface that exceeds what molecular diffusion can transport to and from the surface, so a gradient develops. The result is that the saturation state at the mineral surface, which is what actually determines the surface reaction

rate, is less than it is in the bulk solution. If a complete diffusion control applied, the solution immediately adjacent to the crystal would be at equilibrium with calcite. The coupled diffusion-reaction calculations indicate, however, that the saturation state should be lower next to the crystal than it is in the bulk solution, but not at equilibrium for the 10 μm boundary layer, log Ω = 0.78, while for the 30 μm case, the saturation index decreases to approximately 0.73. These are compared to a log Ω value of just under 0.82 for the bulk solution.

At steady state, the diffusive flux of reactants to and from the mineral surface must balance the rate of reaction at the mineral surface itself. Therefore, the lower rate of reaction associated with a partial diffusion control is captured by the surface reaction-controlled rate immediately adjacent to the mineral, which "sees" the lower saturation state of that microenvironment. Using the calculated lower saturation index from the diffusion boundary layer rather than the values of the saturation index from the bulk solution results in lower precipitation rates than would be predicted by a surface reaction rate control only. For example, in the case of the 30 μm hydrodynamic boundary layer, the calculated value of the saturation index immediately adjacent to the crystal surface of about 0.735 results in a prediction of the rate using Eq. 17 of 1.68×10^{-8} $mol\cdot m^{-2}\cdot s^{-1}$ as compared to a rate of 1.73×10^{-7} $mol\cdot m^{-2}\cdot s^{-1}$ if the bulk solution saturation index of 0.82 for experiment CS-4 from this study applied (i.e., as if no hydrodynamic boundary layer developed). In this way, assuming the Tang et al. [2008a] data describe the surface-reaction controlled rate accurately, one can systematically compute the lower rates that would occur with a 30 μm hydrodynamic boundary layer were present (Table 7 and Figure 13), a situation that likely applies in the case of the largely stagnant flow in the plug-flow column.

Despite the potentially important role of a partial rate control by molecular diffusion in controlling the rate of reactions where large crystals are present, from Figure 11 it is clear that this cannot explain all of the discrepancy between the rates determined in this study and those measured in other studies. The likeliest explanation for most of the discrepancy is that the surface of the calcite spar used in this study has a much lower reactive site density than the calcite seed used in the other studies. A study of calcite

precipitation on Iceland spar conducted by Nehrke et al. [2007] made use of calcite that was essentially identical to that used in the experiments in this study. Nehrke et al. [2007] reported rates ranging from about 10^{-6} to 10^{-7} mol·m^{-2}·s^{-1}, or still 1-2 orders of magnitude faster than those reported here. However, their surface area normalization was based on grain geometry rather than a BET measurement, with the result that their reported specific surface area was about 1-2 orders of magnitude lower than that determined here. Since the Iceland spar used in their experiments is visually almost identical to that used in this study, it seems reasonable to recalculate their rates using the specific surface area determined here to see if this reconciles the apparent discrepancies. Their experiments are complicated by the fact that they considered a range of calcium to carbonate ion activities and their effect on the rate of calcite precipitation (Nehrke et al. [2007], Stack and Grantham [2010], Gebrehiwet et al. [2012]). In this study only a relatively narrow range of calcium to carbonate ion activities from 70-115 was considered [Table 2]. Despite this additional effect, it is clear from Figure 14 that the Nehrke et al. [2007] rates are broadly compatible with those reported here. The reactive site density associated with the Iceland spar used in this and the Nehrke et al. [2007] study is evidently quite different from that of newly nucleated calcite, such as in the Tang et al. [2008a] study.

5.2. Numerical modeling of calcite precipitation in the plug-flow reactor

Reactive transport modeling can be used to test the various rate expressions considered here for calcite precipitation. The objective is to match both the effluent chemistry, which gives the rate of precipitation integrated over the length of the column, and the X-ray microtomography data from column REAC-1. This is done in the simplest case by using the known injection (boundary) and initial conditions from the plug-flow column experiment and incorporating these into a reactive transport simulation that runs for 28 days, the length of the experiment. As a base case, we use an average of 20 $\%_{vol}$ calcite that is distributed evenly over the length of the column and we use the rate expression determined in the stirred reactor experiments (CS-1 to CS-4) and given in Eq. 15. In addition, we assume that the initial and final specific surface area is that of the calcite spar determined by BET method as 0.012 m^2·g^{-1}.

The simulations demonstrate that the nearly linear rate law (n = 1.12) represented by Eq. 15 cannot match the observed distribution of calcium carbonate precipitate when the specific surface area of calcite is held constant at the initial value of 0.012 $m^2 \cdot g^{-1}$ (Figure 15). Specifically, the modeling fails to capture the nonlinear increase in calcium carbonate mass within 1-2 mm of the column inlet.

Several possibilities to improve the match of the reactive transport simulations and the X-ray microtomography data present themselves. One possibility is that the higher specific surface area for newly precipitated calcium carbonate determined in the stirred cell experiments, 0.21 $m^2 \cdot g^{-1}$, should be used. If the higher value is used, then the precipitation of new calcium carbonate in the zone within 1-2 mm of the column inlet is magnified over time. The calcite precipitation profile effectively self-sharpens due to the positive feedback of the high specific surface area generation on the rate of precipitation. Alternatively, the nonlinear profile close to the column inlet might be attributed to the nonlinearity of the rate expressions themselves. In what follows, we first test the various rate expressions by carrying out simulations in which it is assumed that all of the new calcium carbonate has a specific surface area of 0.21 $m^2 \cdot g^{-1}$. In addition to being measured directly in the stirred cell experiments in this study, the higher specific surface value seems reasonable if the newly precipitated calcite consists in part of smaller crystals formed via heterogeneous nucleation.

The data of Tang et al. [2008a] provide a surface reaction controlled rate that can be extended to higher supersaturation than was considered in the stirred cell experiments in this study. If we want to apply this surface reaction controlled rate expression to the coarse crystals present in the plug-flow column experiments in this study, however, it is necessary to factor in the partial diffusion control that reduces those rates in the case of the large seed crystals of calcite and glass beads used in this study. To do this, we fit an effective rate expression to the partial diffusion controlled rates given in Table 7 - here the rate is parameterized in terms of the bulk saturation state (which is the only quantity calculated in this single continuum version of CrunchFlow), but reflects the lower supersaturation expected immediately adjacent to the crystal when a 30 μm hydrodynamic boundary layer is present.

This mixed rate control results in a lower order dependence on the saturation state of the solution, which can be described with the following expression:

$$R = 6.31 \times 10^{-9} \left[\exp\left(\Delta G / R^{*} T \right) - 1 \right]^{2.00} \qquad (18)$$

This effective rate expression can be used to calculate calcium carbonate precipitation rates in a plug-flow column assuming that a 30 μm hydrodynamic boundary layer is present every case surrounding the reacting calcite spar crystals. As discussed in the next section, this reduces the high rates of precipitation one would expect if only a surface reaction rate control were operative.

In Figure 16, a comparison of the reactive transport simulation fit with the X-ray microtomography results after 28 days is shown for three cases, all assuming a value for the specific surface area of newly precipitated calcium carbonate of 0.21 $m^2 \cdot g^{-1}$: i) a profile based on Eq. 15, the best fit to the stirred cell data from this study, with n = 1.12, ii) a profile based on the Tang et al. [2008a] data as represented by Eq. 17, with n = 3.20, and iii) a profile based on a partial diffusion control in which a 30 μm hydrodynamic boundary layer (HBL) is assumed, thus lowering both the rate and the reaction order (n = 2.00, Eq. 18). Neither of the Tang et al. [2008a] based simulations (Figure 16b and c) match the XMT data, as they predict too high a nonlinearity in the profile close to the column inlet. The best match is actually provided by the nearly linear rate expression (Eq. 15) determined from the stirred cell experiments in this study.

Alternatively, it is possible to match the XMT profiles by assuming a constant initial specific surface area of 0.012 $m^2 \cdot g^{-1}$, or if there is a specific surface area increase, it is much closer to the value suggested by the XMT characterization (e.g., 0.025 $m^2 \cdot g^{-1}$). Neither of these scenarios seems reasonable, however, since a higher specific surface area was measured even in the stirred cell experiments (CS-1 to CS-4) that were carried out at lower supersaturation than was achieved near the plug-flow column inlet. The higher value of 0.21 $m^2 \cdot g^{-1}$ seems reasonable given the other measurements of newly precipitated calcite specific surface area in the literature, which range from about 0.19 $m^2 \cdot g^{-1}$ determined by Shiraki and Brantley

[1995] to 0.26 $m^2 \cdot g^{-1}$ determined by Tang et al. [2008a]. Moreover, the higher order dependence on ΔG in the Tang et al. [2008a] study suggests a nucleation mechanism, which implies the rapid generation of new surface area (Steefel and Van Cappellen [1990]), an event that is incompatible with the assumption of a constant and low specific surface area of 0.012 $m^2 \cdot g^{-1}$.

Another possibility that can be tested is whether two calcite precipitation mechanisms operating in parallel can provide a better description of the XMT data. The stirred cell reactor experiments document a linear or nearly linear dependence on Ω that cannot be attributed to even a partial diffusion control, since the surface reaction controlled rates are too slow according to the calculations. A spiral growth mechanism involving multi-source multiple spirals seems most likely, with the overall rate remaining low due to the relative paucity of reactive sites on the spar surface. However, these experiments did not test the entire range of Ω encountered in the REAC-1 experiment that has been the focus of the X-ray microtomography in this study, so it seems reasonable to postulate that more than a single precipitation mechanism was involved in the case of the REAC-1 column, in contrast to the stirred reactor experiments carried out at lower supersaturation. It is postulated that, while a linear or nearly spiral growth mechanism may operate at lower supersaturations, a 2D heterogeneous nucleation mechanism is more important at higher supersaturation. The suggestion of a 2D heterogeneous nucleation mechanism, presumably with a higher order dependence on supersaturation, is reinforced by the observations in Figure 8e and 8f of small 2D nuclei formed on the calcite spar surface, as well as the local growth of calcite crystals directly on glass beads. In addition, the XMT records an increase in specific surface area over the first 1 mm of the column, suggesting that a nucleation event was operative at the higher supersaturations close to the column inlet. To test this hypothesis, we consider a reactive transport simulation in which the higher order nucleation mechanism suggested by the data of Tang et al. [2008a], but modified to include a partial diffusion control according to Eq. 18, is combined with a parallel, nearly linear reaction based on a multi-step spiral growth and described by Eq. 15. When both reaction pathways are included, however, a match with the XMT data is only possible when the diffusion-modified Tang rate constant in Eq. 18 is reduced

to about 2.5×10^{-10} mol·m^{-2}·s^{-1}. Using this value, one obtains the spatial profile shown in Figure 17a, which is in reasonable agreement with the data. The postulated field of dominance of the two mechanisms can be represented by plotting the two parallel rates versus saturation index (log Ω) (Figure 17b).

These simulations results suggest that 2D heterogeneous nucleation, while suggested by direct observation of newly formed crystals and nuclei on both glass bead and calcite spar surfaces and the determination of an increase in specific surface area by both BET and XMT methods, was suppressed in the column relative to what was predicted from the seedless batch experiments of Tang et al. [2008a]. The seedless batch experiments of Tang et al. [2008a] presumably involve a highly transient nucleation stage followed by crystal growth, an interpretation further supported by the observation of a significant decrease in calcite precipitation rates over time in their experiments (Steefel and Van Cappellen [1990]). Both the well stirred and plug-flow reactor experiments in this study are carried out much closer to steady state conditions. A possible conclusion is that while 2D heterogeneous nucleation occurs in the column experiments in particular, it is not a large effect on a mass (or volume) basis.

6. Conclusions

This experimental study highlights the effects of calcite growth on a porous network representing a very simple analogue of sandstone. Both crystal shape and growth rate are strongly dependent on the saturation index and mineral surface nucleation process. Stirred reactor experiments used to provide baseline rates for the coarsely crystalline calcite spar seed material show precipitation rates for calcite with a nearly linear dependence on saturation state, Ω, and at significantly slower rates than measured elsewhere using either no or different seed material. The nearly linear dependence on saturation determined in this study over the range of saturation, log Ω, of 0.15 to 0.82, is likely due to a multiple, multi-sourced spiral growth mechanism (Teng et al. [2000]). Some reconciliation of the Tang et al. [2008a] data with the rates determined in this study is possible by taking into account the partial diffusion control expected for the large seed crystals considered here, which has the effect of suppressing

nucleation to the extent that the supersaturation immediately adjacent to the crystal is lowered. The partial diffusion control is expected to be more important in the case of the more nearly stagnant plug-flow columns, but a discrepancy with the Tang et al. [2008a] batch data persists there as well. However, a good match is obtained with the data in Nehrke et al. [2007], who used seed material essentially identical to that used in this study, if the BET-determined specific surface area determined in this study is used in place of the geometric estimate. The best match with the XMT data, which agrees remarkably well with the spatially integrated rates determined from effluent chemistry in the case of column REAC-1, is provided by either the nearly linear rate law determined in the stirred cell experiments (n = 1.12), or with a combination of nearly linear (multi-sourced spiral growth) and 2D heterogeneous nucleation rate in which the nucleation mechanism is minor on a mass (or volume) basis.

The study indicates that upscaling of calcite precipitation rates to porous samples is possible using data from well-stirred reactor experiments, although it is necessary to account for the evolution of reactivity. The positive feedback between the reactive surface area evolution and the reaction rate results in nonlinear, time-dependent mineral precipitation profile. We expect that upscaling is likely more difficult for natural sub-surface sandstone with hierarchical physical and geochemical heterogeneity structures.

Acknowledgments

This research was supported by the Center for *Nanoscale Control of Geologic* CO_2, an Energy Frontier Research Center funded by the U.S. Department of Energy, Office of Science, Office of Basic Energy Sciences under Award Number DE-AC02-05CH11231. Synchrotron XMT work was performed at the Advanced Light Source, Beamline 8.3.2. Joern Larsen (ESD/LBNL), Alastair MacDowell (ALS/LBNL), Philippe Recourt, Sandra Ventalon and Sylvie Regnier (Université de Lille 1) are thanked for their assistance with ICP-MS, XMT acquisition, SEM, Raman, and preparation of thin sections, respectively.

References

Aagaard, P. and Helgeson, H.C., 1982. Thermodynamic and kinetic constrains on reaction-rates among minerals and aqueous solutions 1. Theoretical considerations. American Journal of Science, 282(3): 237-285.

Blum, A.E. and Lasaga, A.C., 1987. Monte Carlo simulations of surface reaction rate laws. In: W. Stumm (Editor), Aquatic Surface Chemistry: Chemical Processes at the Particle-Water Interface. John Wiley & Sons, New York, pp. 255-292.

Chou, L., Garrels, R.M. and Wollast, R., 1989. Comparative study of the kinetics and mechanisms of dissolution of carbonate minerals. Chemical Geology, 78: 269-282.

Dagan G., 1988. Time-dependent macrodispersion for solute transport in anisotropic heterogeneous aquifers. Water Resources Research, 24: 1491-1500

De Visscher, A. and Vanderdeelen, J., 2003. Estimation of the solubility constant of calcite, aragonite, vaterite, at 25°C based on primary data using the Pitzer ion interaction approach. Chemical Monthly, 134: 769-775.

Dierick, M., Masschaele, B. and Van Hoorebeke, L., 2004. Octopus, a fast and user-friendly tomographic reconstruction package developed in LabView (R). Measurement Science & Technology, 15(7): 1366-1370.

Giambalvo, E.R., Steefel, C.I., Fisher, A.T., Rosenberg, N.D. and Wheat, C.G., 2002. Effect of fluid-sediment reaction on hydrothermal fluxes of major elements, eastern flank of the Juan de Fuca Ridge. Geochimica Et Cosmochimica Acta, 66(10): 1739-1757.

Gebrehiwet, T.A., Redden, G.D., Fujita, Y., Belg, M.S., Smith, R.W., 2012. The effects of the CO_3^{2-} to Ca^{2+} ion activity ratio on calcite precipitation kinetics and Sr^{2+} partitioning. Geochemical Transactions, 13: 1, doi:10.1186/1467-4866-13-1.

Gelhar, L.W., 1986. Stochastic subsurface hydrology from theory to applications. Water Resources Research, 22: 135S-145S

Gonzales, R.C. and Woods, R.E., 1992. Digital image processing. Addison-Wesley Publishing Compagny, Reading, Massachusetts, 716 pp.

Hassenkam, T., Johnsson, A., Bechgaard, K. and Stipp, S.L.S., 2011. Tracking single coccolith dissolution with picogram resolution and implications for CO(2) sequestration and ocean acidification. Proceedings of the National Academy of Sciences of the United States of America, 108(21): 8571-8576.

Hintz, R.J. and Johnson, K.C., 1989. The effect of particle size distribution on dissolution rate and oral absorption. International Journal of Pharmaceutics, 51(1): 9-17.

Inskeep, W.P. and Bloom, P.R., 1985. An evaluation of rate-equations for calcite precipitation kinetics at PCO2 less than 0.01atm and pH greater than 8. Geochimica Et Cosmochimica Acta, 49(10): 2165-2180.

Lasaga, A.C., 1998. Kinetic theory in the earth sciences. Princeton University Press, New Jersey, 811 pp.

Lasaga, A.C., 1981. Rate laws in chemical reactions. *In* Kinetics of Geochemical Processes. Vol 8, A.C. Lasaga and R.J. Kirkpatrick (eds). Mineralogical Society of America, 135-169.

Li, L., Peters, C.A. and Celia, M.A., 2006. Upscaling geochemical reaction rates using pore-scale network modeling. Advances in Water Resources, 29(9): 1351-1370.

Li, L., Steefel, C.I. and Yang, L., 2008. Scale dependence of mineral dissolution rates within single pores and fractures. Geochimica et Cosmochimica Acta, 72(2): 360-377.

Maher, K., Steefel, C.I., White, A.F. and Stonestrom, D.A., 2009. The role of reaction affinity and secondary minerals in regulating chemical weathering rates at the Santa Cruz Soil Chronosequence, California. Geochimica Et Cosmochimica Acta, 73(10): 2804-2831.

Nancollas, G. and Reddy, M.M., 1971. Crytallization of calcium carbonate 2. Calcite growth mechanism. Journal of Colloid and Interface Science, 37(4): 824-830.

Nehrke, G., Reichart, G.J., Van Cappellen, P., Meile, C., Bijma, J., 2007. Dependence of calcite growth rate and Sr partitioning on solution stoichiometry: Non-Kossel crystal growth. Geochimica Et Cosmochimica Acta, 71: 2240-2249.

Nielsen, A.E., 1984. Electrolyte crystal-growth mechanisms. Journal of Crystal Growth, 67(2): 289-310.

Noiriel, C., Bernard, D., Gouze, P. and Thibaut, X., 2005. Hydraulic properties and microgeometry evolution in the course of limestone dissolution by CO2-enriched water. Oil & Gas Science and Technology, 60(1): 177-192.

Noiriel, C., Gouze, P. and Bernard, D., 2004. Investigation of porosity and permeability effects from microstructure changes during limestone dissolution. Geophysical Research Letters, 31(24): L24603, doi:10.1029/2004GL021572.

Oelkers, E.H., Schott, J. and Devidal, J.L., 1994. The effect of aluminium, pH, and chemical affinity on the rates of aluminosilicate dissolution reactions. Geochimica Et Cosmochimica Acta, 58(9): 2011-2024.

Pokrovsky, O.S., Golubev, S.V. and Schott, J., 2005. Dissolution kinetics of calcite, dolomite and magnesite at 25 degrees C and 0 to 50 atm pCO(2). Chemical Geology, 217(3-4): 239-255.

Ranz, W.E. and Marshall, W.R., 1952. Evaporation from drops 1. Chemical Engineering Progress, 48(3): 141-146.

Shiraki, R. and Brantley, S.L., 1995. Kinetics of near-equilibrium calcite precipitation at 100°C - An evaluation of elementary reaction-based and affinity-based rate laws. Geochimica Et Cosmochimica Acta, 59(8): 1457-1471.

Stack, A.G. and Grantham, M.C., 2010. Growth rate of calcite steps as a function of aqueous calcium-to-carbonate ratio: Independent attachment and detachment of calcium and carbonate ions. Crystal Growth and Design, 10: 1409-1413.

Steefel, C.I., DePaolo, D.J. and Lichtner, P.C., 2005. Reactive transport modeling: An essential tool and a new research approach for the Earth sciences. Earth and Planetary Science Letters, 240(3-4): 539-558.

Steefel, C.I. and Lasaga, A.C., 1990. Evolution of dissolution patterns: Permeability change due to coupled flow and reaction. In: D. Melchior and R.L. Bassett (Editors), Chemical Modeling of Aqueous Systems II. American Chemical Society, Washington DC, pp. 212-225.

Steefel, C.I. and Lasaga, A.C., 1994. A coupled model for transport of multiple chemical species and kinetic precipitation/dissolution reactions with application to reactive flow in single phase hydrothermal systems. . American Journal of Science 294: 529-592.

Steefel, C.I. and Lichtner, P.C., 1994. Diffusion and reaction in rock matrix bordering a hyperalkaline fluid-filled fracture. Geochimica et Cosmochimica Acta, 58(17): 3595-3612.

Steefel, C.I. and Maher, K., 2009. Fluid-Rock Interaction: A Reactive Transport Approach. In: E.H. Oelkers and J. Schott (Editors), Thermodynamics and Kinetics of Water-Rock Interaction. Reviews in Mineralogy & Geochemistry. Mineralogical Soc Amer, Chantilly, pp. 485-532.

Steefel, C.I. and Van Cappellen, P., 1990. A new kinetic approach to modeling water-rock interaction - The role of nulceation, precursors, and Ostwald ripening. Geochimica Et Cosmochimica Acta, 54(10): 2657-2677.

Sugano, K., 2008. Theoretical comparison of hydrodynamic diffusion layer models used for dissolution simulation in drug discovery and development. International Journal of Pharmaceutics, 363(1-2): 73-77.

Tang, J.W., Dietzel, M., Bohm, F., Kohler, S.J. and Eisenhauer, A., 2008a. Sr(2+)/Ca(2+) and (44)Ca/(40)Ca fractionation during inorganic calcite formation: II. Ca isotopes. Geochimica Et Cosmochimica Acta, 72(15): 3733-3745.

Tang, J.W., Kohler, S.J. and Dietzel, M., 2008b. Sr2+/Ca2+ and Ca-44/Ca-40 fractionation during inorganic calcite formation: I. Sr incorporation. Geochimica Et Cosmochimica Acta, 72(15): 3718-3732.

Teng, H.H., Dove, P.M. and De Yoreo, J.J., 2000. Kinetics of calcite growth: Surface processes and relationships to macroscopic rate laws. Geochimica Et Cosmochimica Acta, 64(13): 2255-2266.

White, A.F. and Brantley, S.L., 2003. The effect of time on the weathering of silicate minerals: why do weathering rates differ in the laboratory and field? Chemical Geology, 202: 479-506.

Wolery, T.J. et al., 1990. Current status of the EQ3/6 software package for geochemical modeling. Acs Symposium Series, 416: 104-116.

Figure Captions

Figure 1. Scanning electron microscope (SEM) images of (a) glass beads and (b) and (c) calcite crystal before experiments.

Figure 2. Schematic of the plug-flow column experimental setup.

Figure 3. XMT cross-section (256×256 pixels) of the sample REAC-1 (a) Initial 256-grey levels image and (b) image after segmentation, identifying porosity (black), calcite (grey) and glass bead (white).

Figure 4. Saturation index (log Ω) versus rate for the stirred cell experiments in this study.

Figure 5. Changes in effluent Ca (a) and pH (b) for columns REAC-0, REAC-1, and REAC-2.

Figure 6. Calcium carbonate precipitated within REAC-1 column after 28 days based on XMT. The column inlet is on the left, the exit on the right.

Figure 7. XMT small 3D volumes (256×256×128 pixels) of the sample REAC-1 showing the precipitation of calcite and the shift of the fluid-rock interface. (a) Sample before experiment, showing glass beads (royal blue) and calcite (sky blue). (b), Sample after experiment, (c) Sample

after experiment, showing the displacement of the fluid-rock interface during experiment. White and yellow lines correspond to the position of the fluid-rock interface (in the foreground slice) at t_0 and t_1, respectively. Note that the interface mismatch for the right-bottom glass bead is due to bead displacement during experiment.

Figure 8. SEM pictures of sample REAC-1 after experiment. Calcite crystals grew on glass bead surface (a) and (b), calcite spar surface close to the sample inlet (c) and (d), and close to the sample outlet (e) and (f).

Figure 9. XMT cross-sections of sample REAC-1 before and after experiment showing roughness increase

Figure 10. Specific surface area changes in REAC-1 based on XMT (spatial resolution of 4.46 μm).

Figure 11. Comparison of calcite precipitation rates from this study and that of Tang et al. [2008a]

Figure 12. 10 and 30 μm boundary layers for the case of CS-4 with a bulk saturation index of 0.82. The modeling assumes that the Tang et al. [2008a] rate applies at the mineral surface. The gradient indicates a partial diffusion control. See text for further explanation.

Figure 13. Tang rates recalculated for a partial diffusion control assuming a 30 μm thick hydrodynamic boundary layer.

Figure 14: Comparison of calcite growth rate data from Nehrke et al. [2007] (blue symbols) and this study (red symbols and fitted curve). Nehrke et al. [2007] considered a broad range of calcium to carbonate ion activity ratios (unlike this study), which accounts for some of the spread in their data when plotted versus log Ω alone.

Figure 15. Fit of XMT data with the nearly linear rate expression (n = 1.12) determined in stirred cell reactor experiments from this study and using a constant initial specific surface area of 0.012 $m^2 \cdot g^{-1}$.

Figure 16. Reactive transport simulation matching of XMT profiles (red data points) of newly precipitated calcium carbonate with a specific surface area of 0.21 $m^2 \cdot g^{-1}$. Plug-flow column inlet is on the left. (a) Simulated profile (dark blue solid line) with n = 1.12 using Eq. 15, (b) simulated profile (dark blue solid line) with model fit to Tang et al. [2008a] data, n = 3.20 (Eq. 17), and (c) simulated profile (dark blue solid line) with model fit to Tang data adjusted for a partial diffusion control based on a 30 μm hydrodynamic boundary layer (Eq. 18).

Figure 17. (a) Comparison of simulated profile of newly precipitated calcium carbonate with XMT data when two parallel rate laws are combined: 1) a partially diffusion controlled modification of the higher order rate expression suggested by Tang et al. [2008a] data, and 2) the nearly linear (n=1.12) multi-sourced spiral growth mechanism suggested by the stirred cell experiments in this study. The rates fromTang et al. [2008a], however, need to be slowed even beyond the modification imposed by a partial diffusion control in order to result in a reasonable match with the data. (b)

Postulated precipitation rate regimes based on plug-flow column experiments: spiral growth controlled (dark solid line) vs nucleation control (grey solid line).

Table 1. Chemical composition of initial calcite material.

Element	[Ca]	[Mg]	[Sr]	[Ba]	[K]	[Na]	[Si]	[Al]	[Rb]
Concentration (% weight)	39.33	0.14	0.02	0.27	0.08	0.03	1.52	0.03	0.02

Table 2. Summary of the continuously-stirred precipitation experiments

Experiment	SC-1	SC-2	SC-3	SC-4
pH_{in}	8.16	8.41	8.25	8.20
pH_{out}	7.97	7.99	8.032	7.89
DIC_{in}[a] ($mmol \cdot l^{-1}$)	2.120	4.077	2.987	6.278
DIC_{out} ($mmol \cdot l^{-1}$)	1.987	3.509	2.709	4.942
Ca_{in}[c] ($mmol \cdot l^{-1}$)	1.071	2.043	1.436	4.000
Ca_{out}[d] ($mmol \cdot l^{-1}$)	0.938	1.475	1.158	2.664
ΔCa ($mmol \cdot l^{-1}$)	0.133	0.568	0.278	1.336
Calcite Ppt (g)	0.0046	0.0143	0.0033	0.0192
Calcite SSA_{fin}[f] ($m^2 \cdot g^{-1}$)	0.013	0.015	0.013	0.016
aCa^{2+} / aCO_3^{2-}	94.9	74.7	70.9	115
Log Ω[e]	0.15	0.57	0.42	0.82
Log R ($mol \cdot m^{-2} \cdot s^{-1}$)	-8.89	-8.26	-8.49	-7.91

a. DIC in well-mixed stock solution based on average of 3 Na analyses by ICP-MS, with assumption that total Na = total Dissolved Inorganic Carbonate (DIC).

b. DIC from effluent not measured directly, but estimated by subtracting the Ca precipitated in the reactor ($\Delta Ca = \Delta DIC$) from the DIC in the well-mixed stock solution.

c. Average of 3-4 ICP-MS measurements of total Ca in well mixed stock.

d. Average of 5-15 Ca values determined by ICP-MS at steady state

e. Calculated with CrunchFlow using the EQ3 database (Wolery et al. [1990]). Makes use of the extended Debye-Huckel model for activity corrections. Thermodynamic data at 22°C given in Table 3.

f. Final surface area calculated from the weighted fraction of original Iceland spar (1.0 g) and the new calcite precipitate using a multipoint krypton gas BET method.

Table 3. Thermodynamic data at 22°C used in simulations. Note that the primary species used in the calculation are Ca^{2+} and CO_3^{2-}.

Species	Log K	Species	Log K
HCO_3^-	-10.352	$CO_{2(aq)}$	-16.712
$CaCl^+$	0.70339	$CaCO_{3(aq)}$	-3.2881
$CaCl_{2(aq)}$	0.64203	$CaHCO_3^+$	-11.393
$HCl_{(aq)}$	-0.69908	$NaCO_3^-$	-0.54579
$NaCl_{(aq)}$	0.79087	$NaHCO_{3(aq)}$	-10.532
$NaOH_{(aq)}$	14.894	Calcite	-8.4521
OH^-	14.091	Vaterite	-7.927

Table 4. Composition of the plug-flow columns.

Sample name	REAC-0	REAC-1	REAC-2
mass (g)	0.5767	0.6300	0.6541
calcite (%w)	0	25	25
glass beads (%w)	100	75	75

Table 5. Composition of the inlet fluid after mixing for the plug-flow column experiments

Sample name	REAC-0	REAC-1	REAC-2
$CaCl_2$ (mM)	2.0 ± 0.1	2.0 ± 0.1	1.0 ± 0.1
$NaHCO_3$ (mM)	4.0 ± 0.1	4.0 ± 0.1	2.0 ± 0.1
Log Ω	1.44	1.44	0.69
pH_{in}	8.70	8.70	8.45

Table 6. Diffusion coefficients used in reactive transport modelling

Ion	D_i ($\times 10^5$ $cm^2 \cdot s^{-1}$)	Ion	D_i ($\times 10^5$ $cm^2 \cdot s^{-1}$)
H^+	9.31*	OH^-	5.27*
Na^+	1.33*	Cl^-	2.03*
Ca^{2+}	0.793*	HCO_3^-	1.18*
$CO_{2(aq)}$	1.00	CO_3^{2-}	0.955*
$CaCl^{2+}$	1.00	$CaCl_{2(aq)}$	1.00
$CaCO_{3(aq)}$	1.00	$CaHCO_3^+$	1.00
$NaCO_3^-$	1.00	$NaHCO_{3(aq)}$	1.00

*Data from Lasaga [1998]; otherwise a value is assumed.

Table 7. 25°C calcite precipitation rates from Tang et al. [2008a] recalculated for a partial diffusion control assuming a 30 μm thick hydrodynamic boundary layer.

	[a]log Ω (at crystal surface)	[b]log Ω (bulk solution)	[c]Crystal surface rate ($mol \cdot m^{-2} \cdot s^{-1}$)	[d]Bulk rate ($mol \cdot m^{-2} \cdot s^{-1}$)	log crystal surface rate ($mol \cdot m^{-2} \cdot s^{-1}$)	log bulk rate ($mol \cdot m^{-2} \cdot s^{-1}$)
Tang-11	0.963	1.192	1.156×10^{-6}	7.330×10^{-6}	-5.937	-5.135
Tang-12	0.922	1.095	8.260×10^{-7}	3.396×10^{-6}	-6.083	-5.469
Tang-13	0.928	1.108	8.649×10^{-7}	3.771×10^{-6}	-6.063	-5.424
Tang-14	0.836	0.931	3.986×10^{-7}	8.868×10^{-7}	-6.399	-6.052
Tang-15	0.638	0.660	6.630×10^{-8}	8.171×10^{-8}	-7.178	-7.088
Tang-16	0.806	0.882	3.059×10^{-7}	5.882×10^{-7}	-6.514	-6.230
Tang-17	0.630	0.651	6.146×10^{-8}	7.490×10^{-8}	-7.211	-7.126
Tang-18	0.655	0.680	7.794×10^{-8}	9.837×10^{-8}	-7.108	-7.007
Tang-19	0.965	1.200	1.182×10^{-6}	7.806×10^{-6}	-5.927	-5.108
Tang-20	0.929	1.111	8.707×10^{-7}	3.844×10^{-6}	-6.060	-5.415
Tang-21	0.977	1.233	1.302×10^{-6}	1.010×10^{-5}	-5.885	-4.995
Tang-22	0.912	1.073	7.551×10^{-7}	2.834×10^{-6}	-6.122	-5.548
Tang-23	0.735	0.780	1.630×10^{-7}	2.443×10^{-7}	-6.788	-6.612

a. Saturation index calculated with the Tang et al [2008a] surface reaction rate (Eq. 17) and multicomponent diffusion across a 30 μm hydrodynamic boundary layer using coefficients in Table 6.

b. Saturation index calculated with the Tang et al [2008a] surface reaction rate (Eq. 17) assuming the bulk solution is present immediately adjacent to the calcite crystal (no hydrodynamic boundary layer).

c. Rate calculated from Eq. 17 assuming the saturation state immediately adjacent to the calcite surface is given by the log Ω values given in Column a.

d. Rate calculated from Eq. 17 assuming that the bulk solution (Column b) is immediately adjacent to the calcite surface.

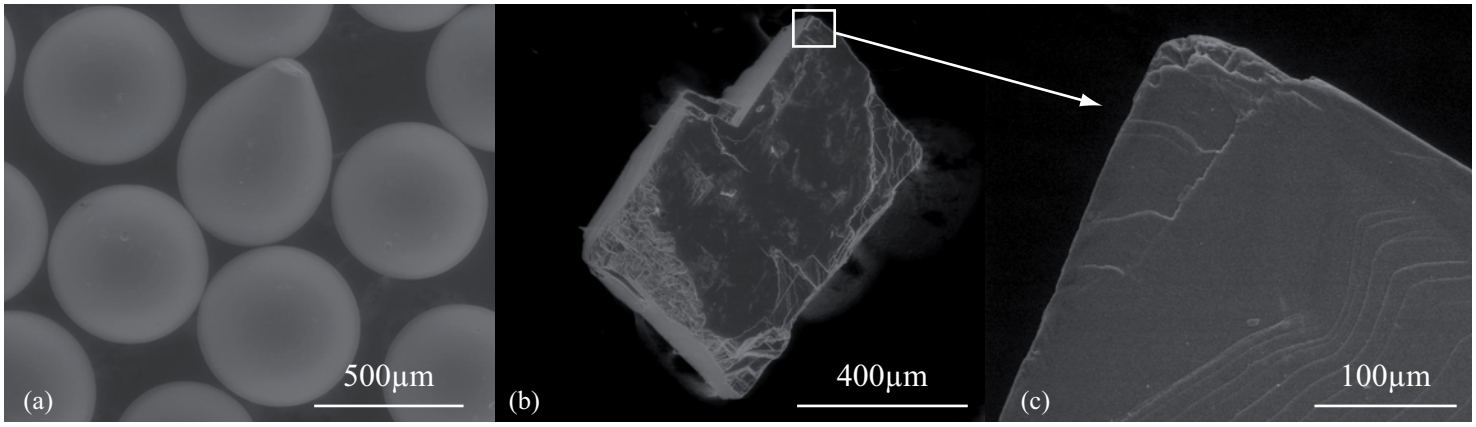

Figure 1. Scanning electron microscope (SEM) images of (a) glass beads and (b) and (c) calcite crystal before experiments.

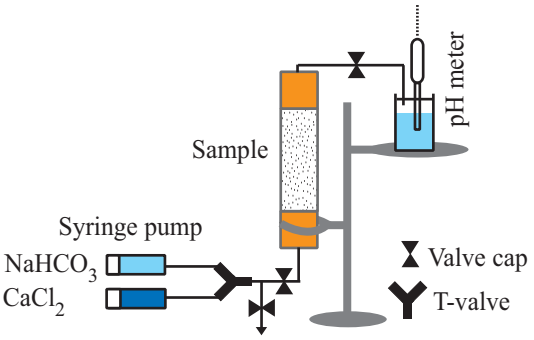

Figure 2. Schematic of the plug-flow column experimental setup

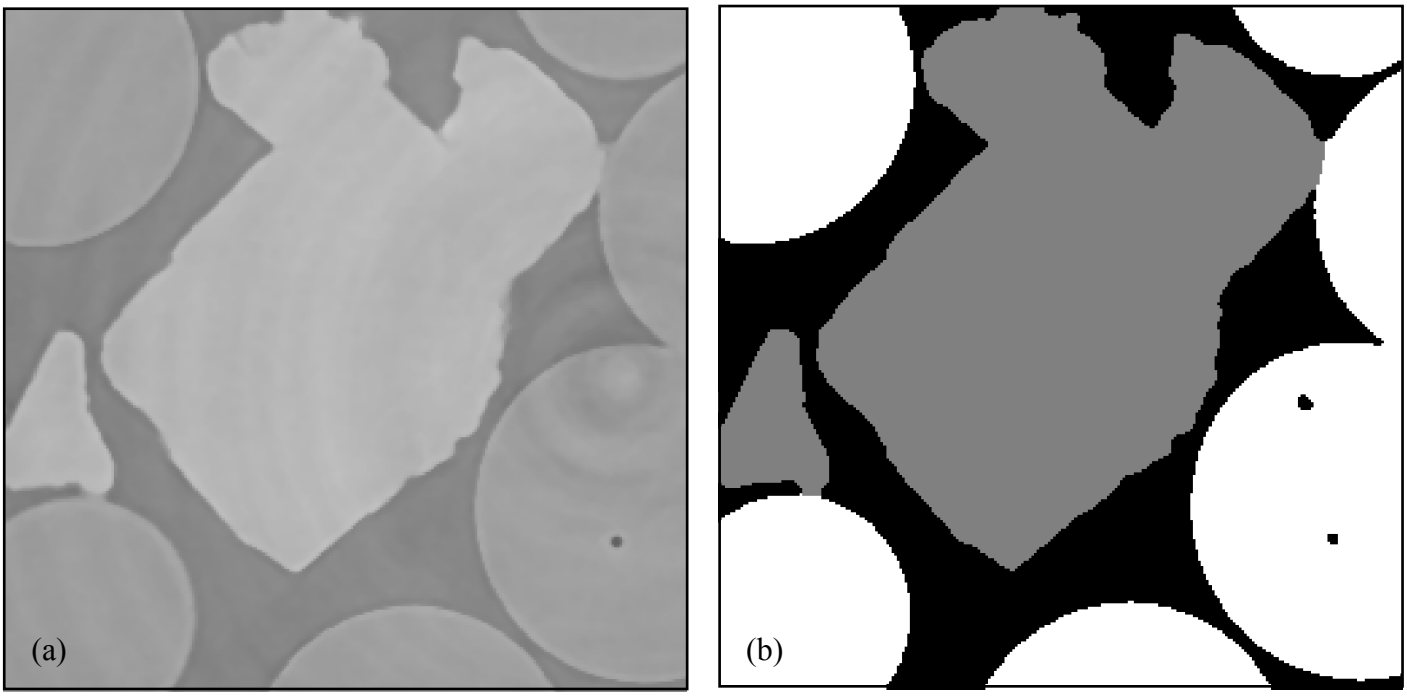

Figure 3. XMT cross-section (256×256 pixels) of the sample REAC-1 (a) Initial 256-grey levels image and (b) image after segmentation, identifying porosity (black), calcite (grey) and glass bead (white).

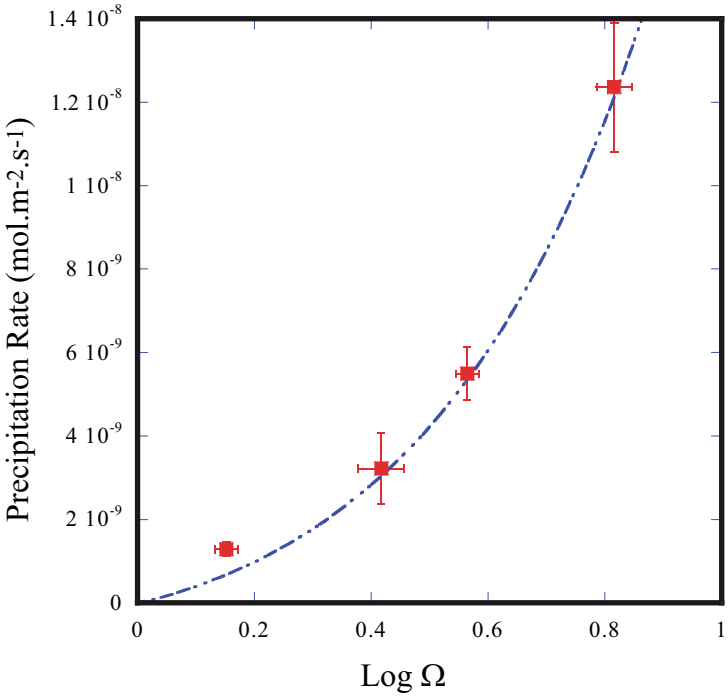

Figure 4. Saturation index (log Ω) versus rate for the stirred cell experiments in this study

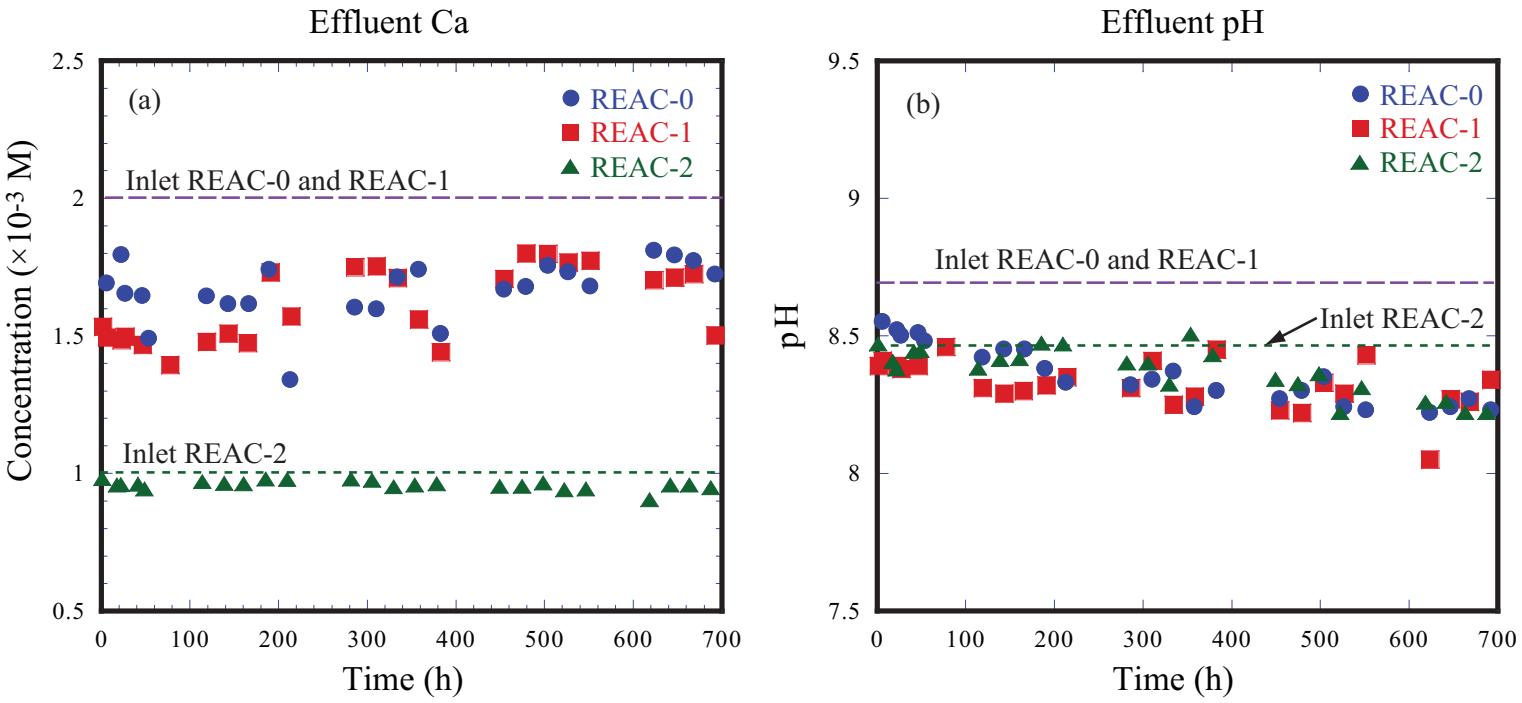

Figure 5. Changes in effluent Ca (a) and pH (b) for columns REAC-0, REAC-1, and REAC-2.

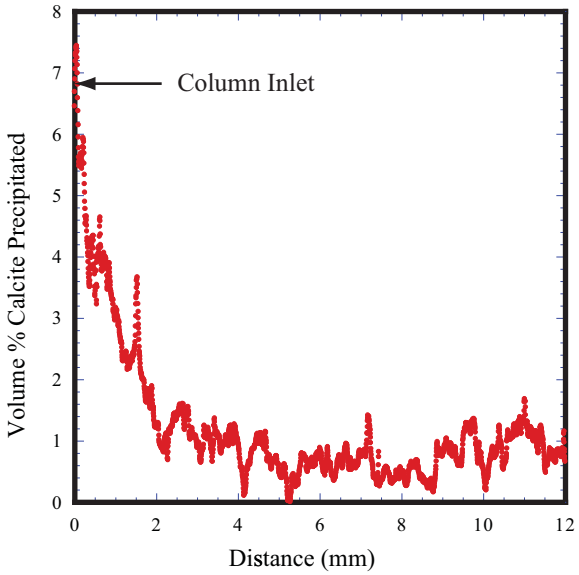

Figure 6. Calcium carbonate precipitated within REAC-1 column after 28 days based on XMT. The column inlet is on the left, the exit on the right.

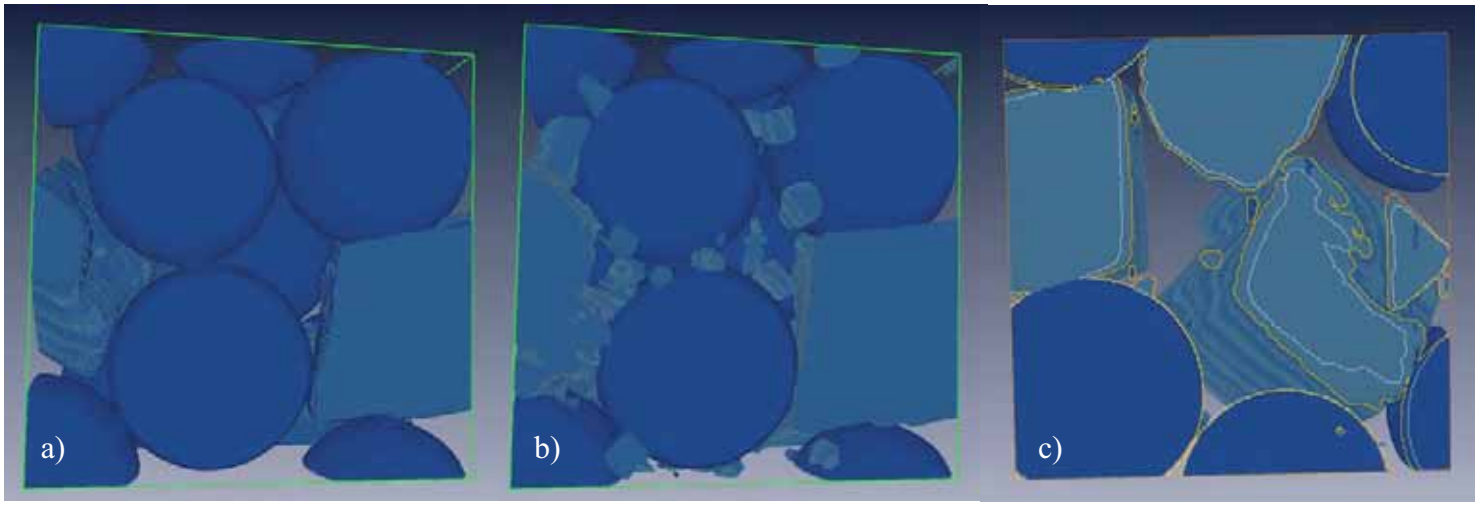

Figure 7. XMT small 3D volumes (256×256×128 pixels) of the sample REAC-1 showing the precipitation of calcite and the shift of the fluid-rock interface. (a) Sample before experiment, showing glass beads (royal blue) and calcite (sky blue). (b), Sample after experiment, (c) Sample after experiment, showing the displacement of the fluid-rock interface during experiment. White and yellow lines correspond to the position of the fluid-rock interface (in the foreground slice) at t_0 and t_1, respectively. Note that the interface mismatch for the right-bottom glass bead is due to bead displacement during experiment.

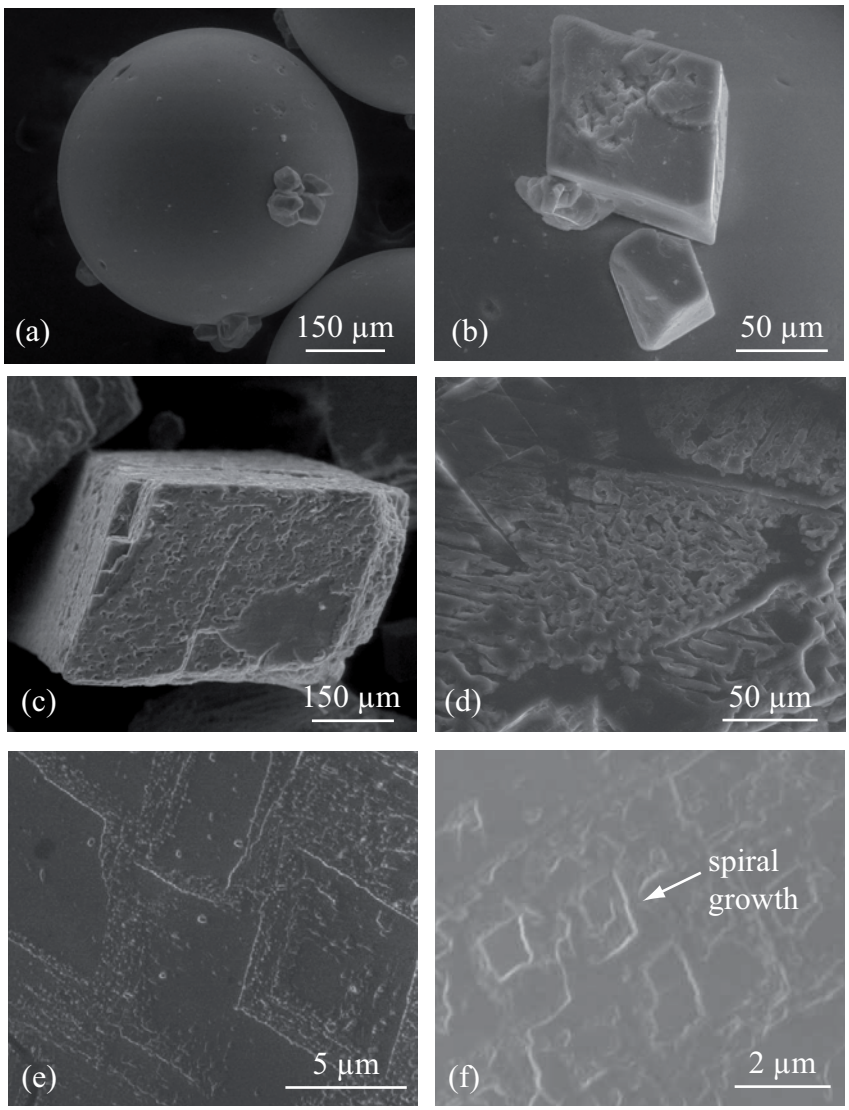

Figure 8. SEM pictures of sample REAC-1 after experiment. Calcite crystals grew on glass bead surface (a) and (b), calcite spar surface close to the sample inlet (c) and (d), and close to the sample outlet (e) and (f).

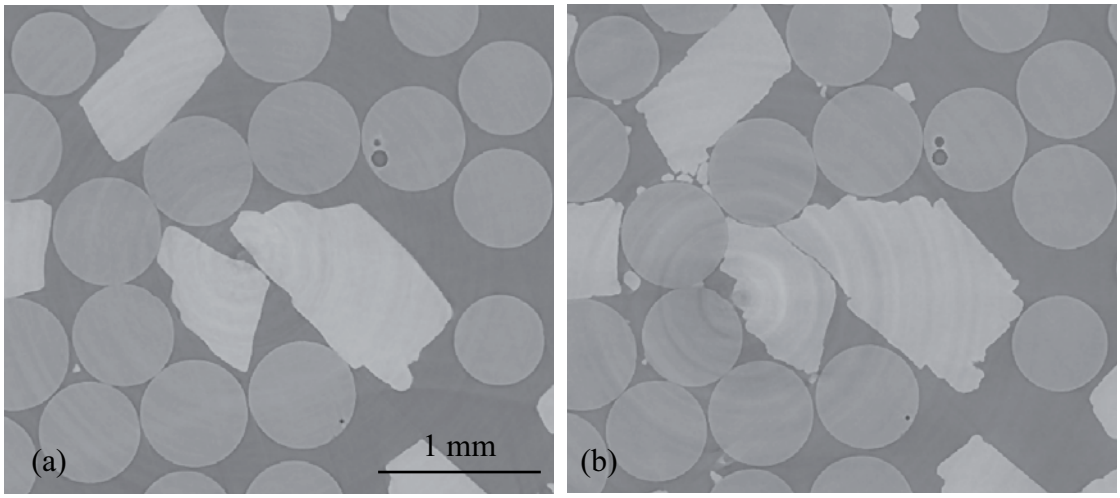

Figure 9. XMT cross-sections of sample REAC-1 before and after experiment showing roughness increase

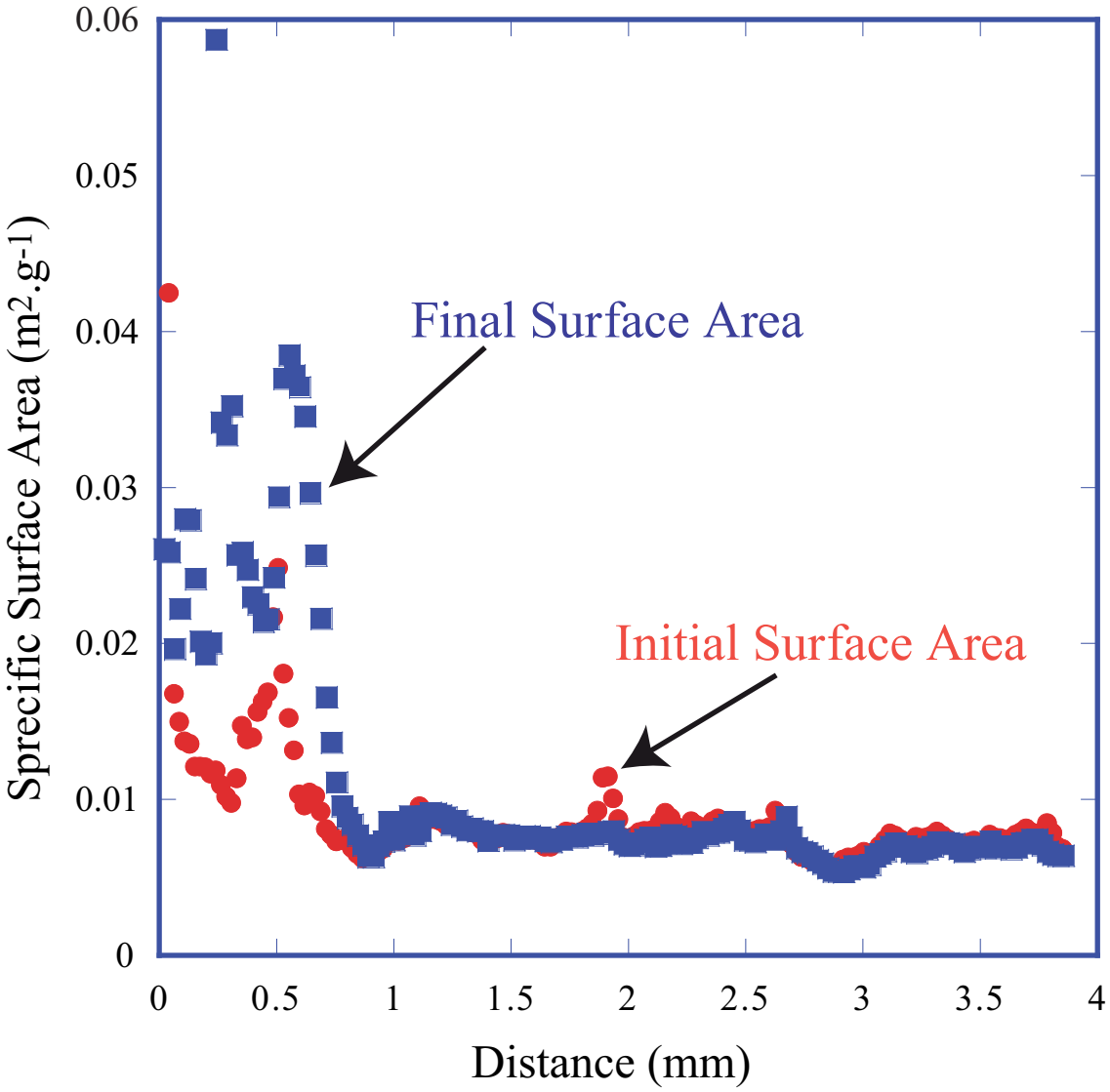

Figure 10. Specific surface area changes in REAC-1 based on XMT (spatial resolution of 4.46 µm).

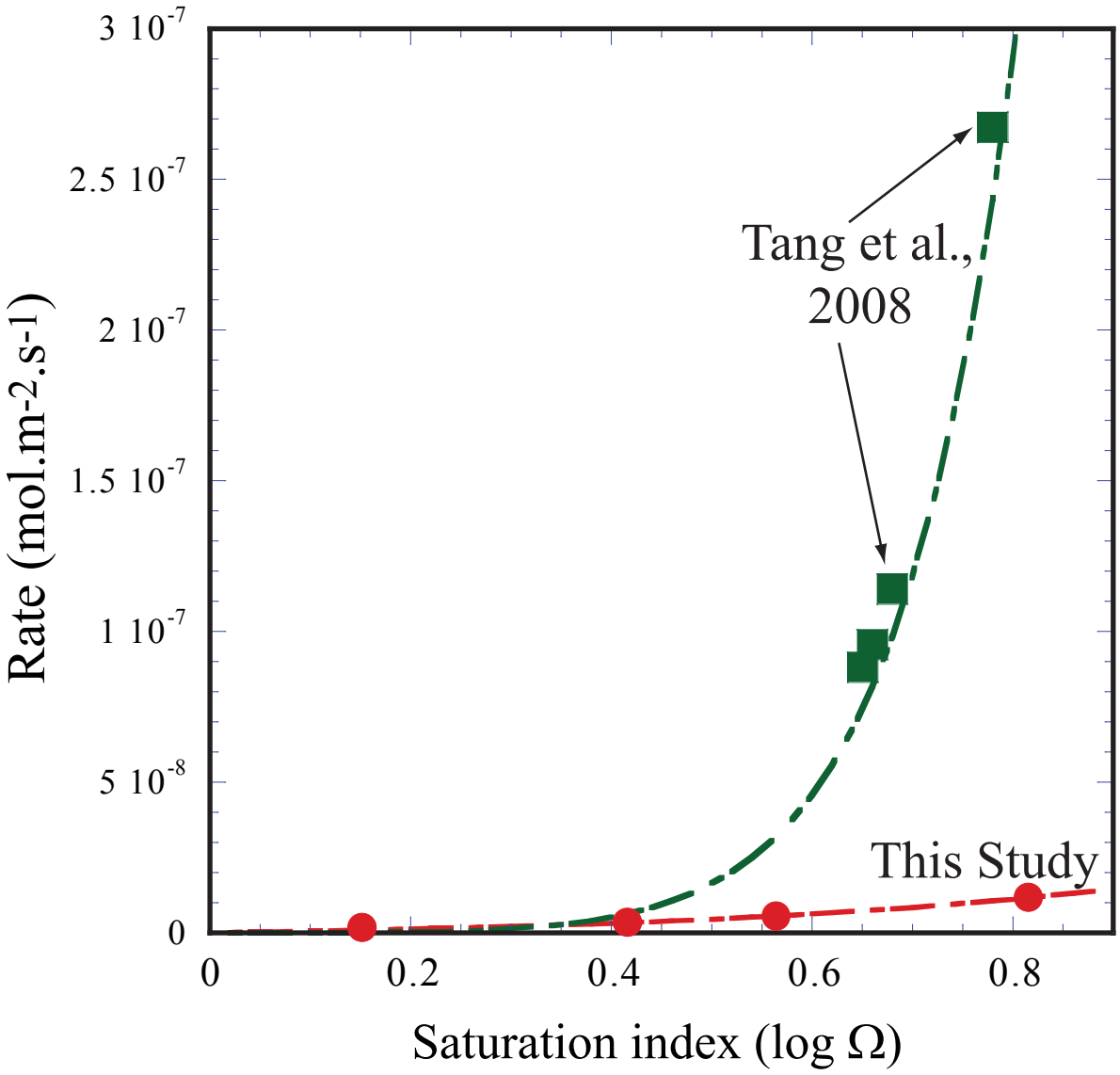

Figure 11. of calcite precipitation rates from this study and that of Tang et al. [2008a]

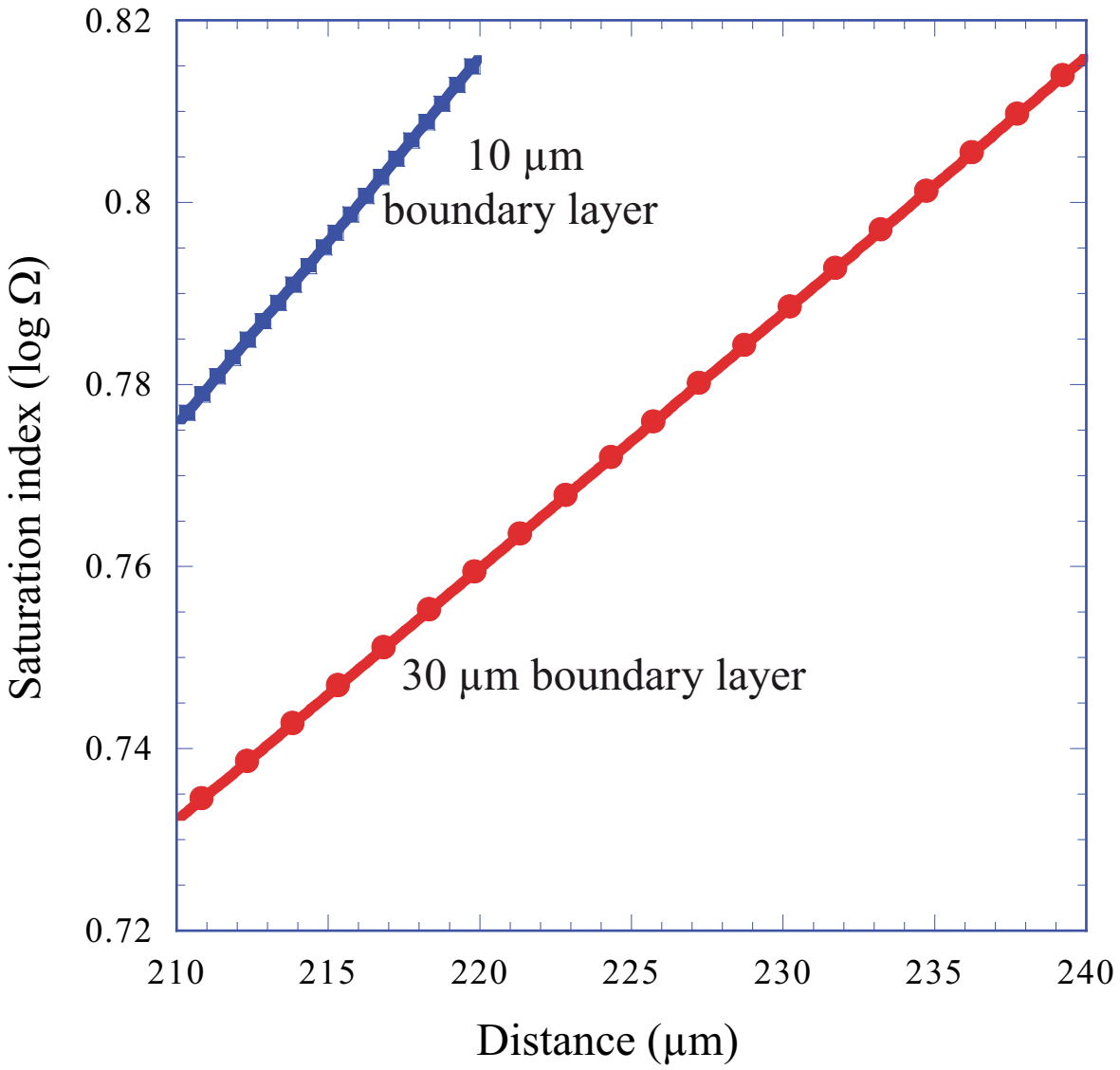

Figure 12. 10 and 30 μm boundary layers for the case of CS-4 with a bulk saturation index of 0.82. The modeling assumes that the Tang et al. [2008a] rate applies at the mineral surface. The gradient indicates a partial diffusion control. See text for further explanation.

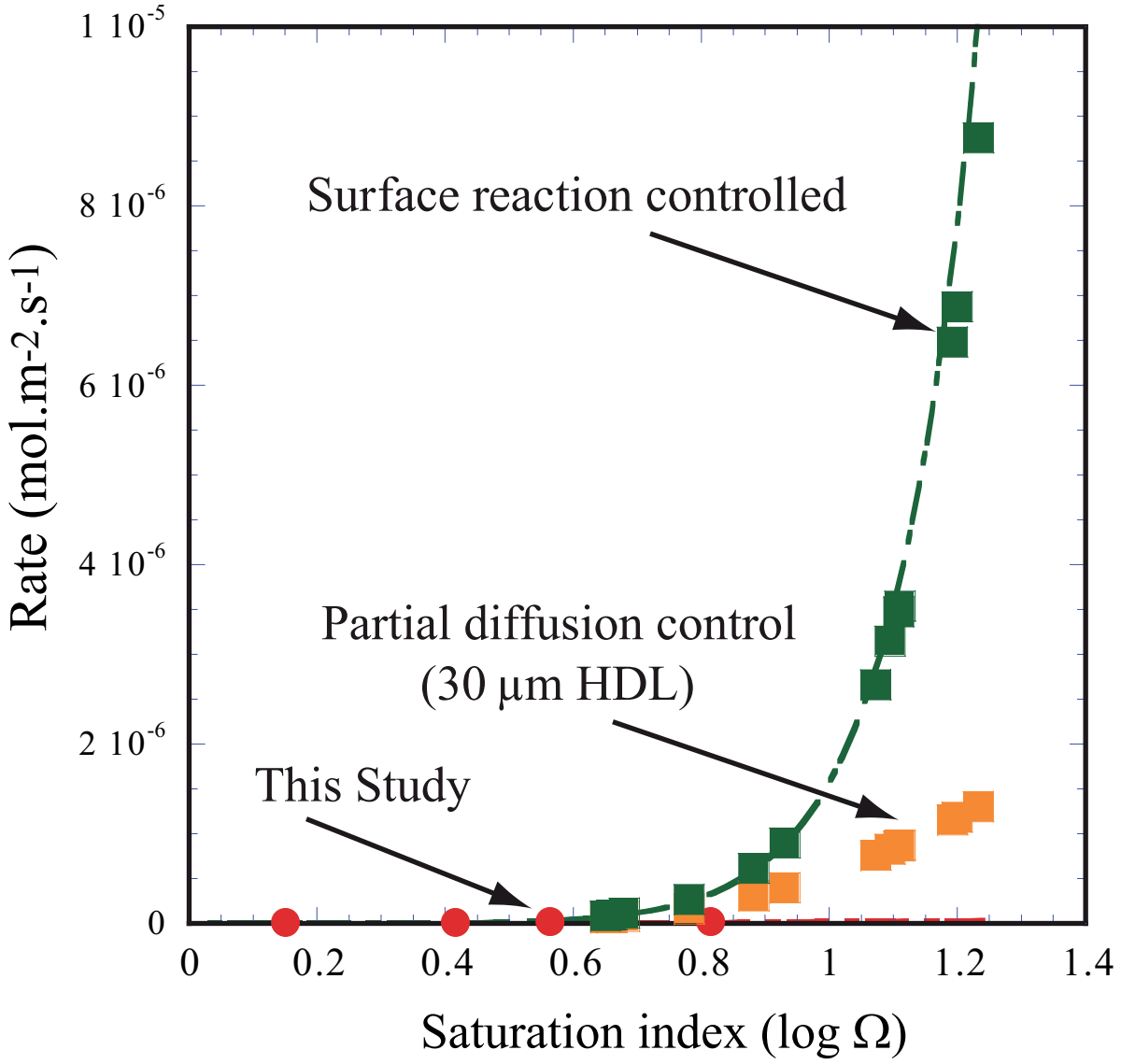

Figure 13. Tang rates recalculated for a partial diffusion control assuming a 30 µm thick hydrodynamic boundary layer.

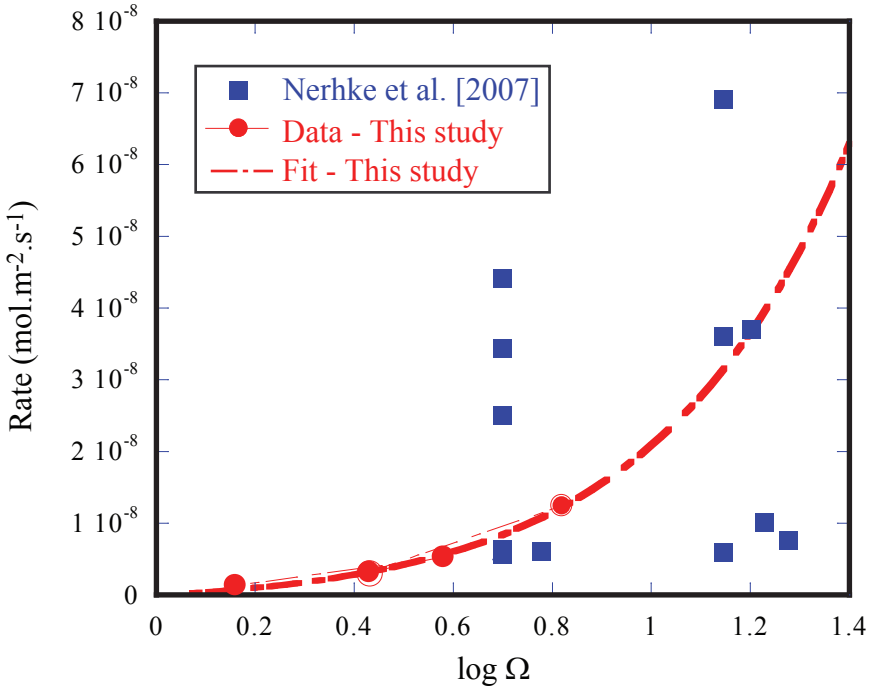

Figure 14. Comparison of calcite growth rate data from Nehrke et al. [2007] (blue symbols) and this study (red symbols and fitted curve). Nehrke et al. [2007] considered a broad range of calcium to carbonate ion activity ratios (unlike this study), which accounts for some of the spread in their data when plotted versus log Ω alone.

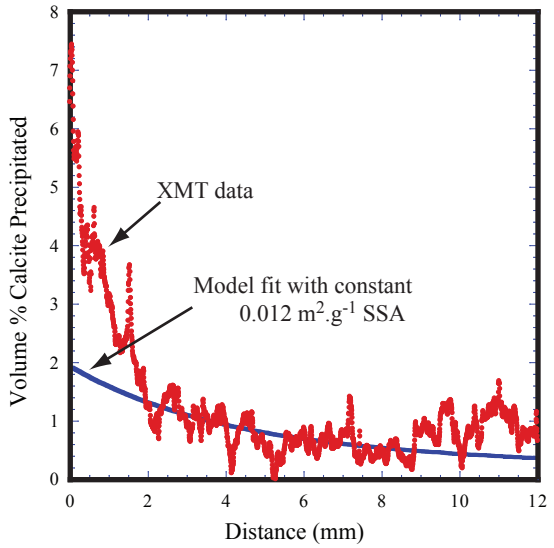

Figure 15. Fit of XMT data with the nearly linear rate expression (n = 1.12) determined in stirred cell reactor experiments from this study and using a constant initial specific surface area of 0.012 m2·g-1.

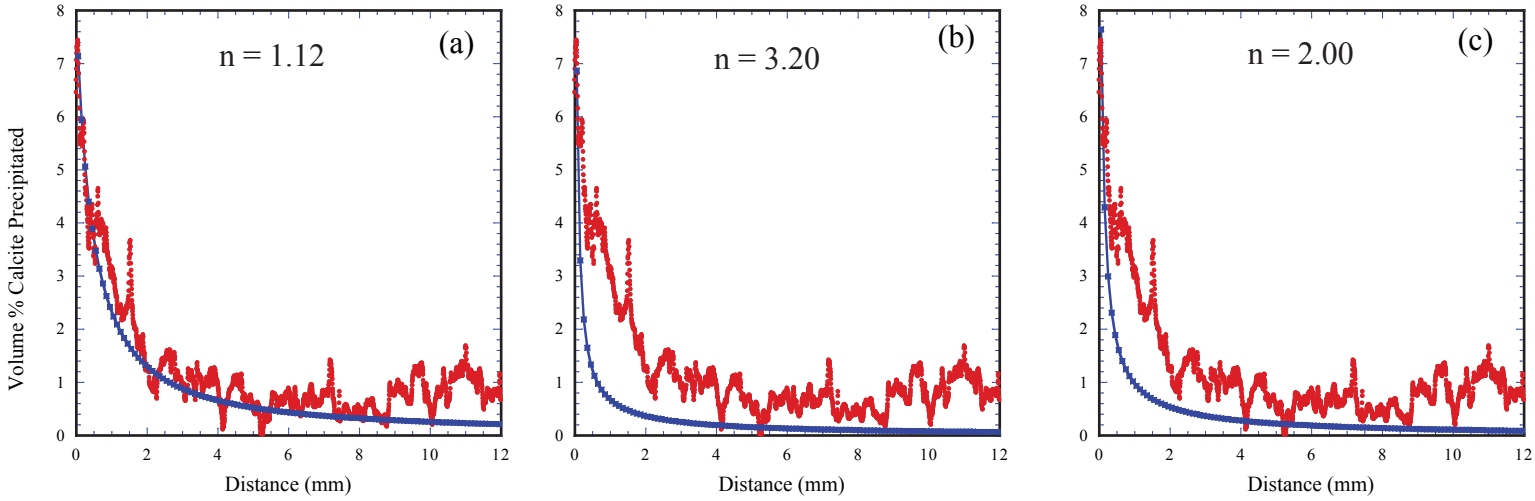

Figure 16. Reactive transport simulation matching of XMT profiles (red data points) of newly precipitated calcium carbonate with a specific surface area of 0.21 m2·g-1. Plug flow column inlet is on the left. (a) Simulated profile (dark blue solid line) with n = 1.12 using Eq. 15, (b) simulated profile (dark blue solid line) with model fit to Tang et al. [2008a] data, n = 3.20 (Eq. 17), and (c) simulated profile (dark blue solid line) with model fit to Tang data adjusted for a partial diffusion control based on a 30 µm hydrodynamic boundary layer (Eq. 18).

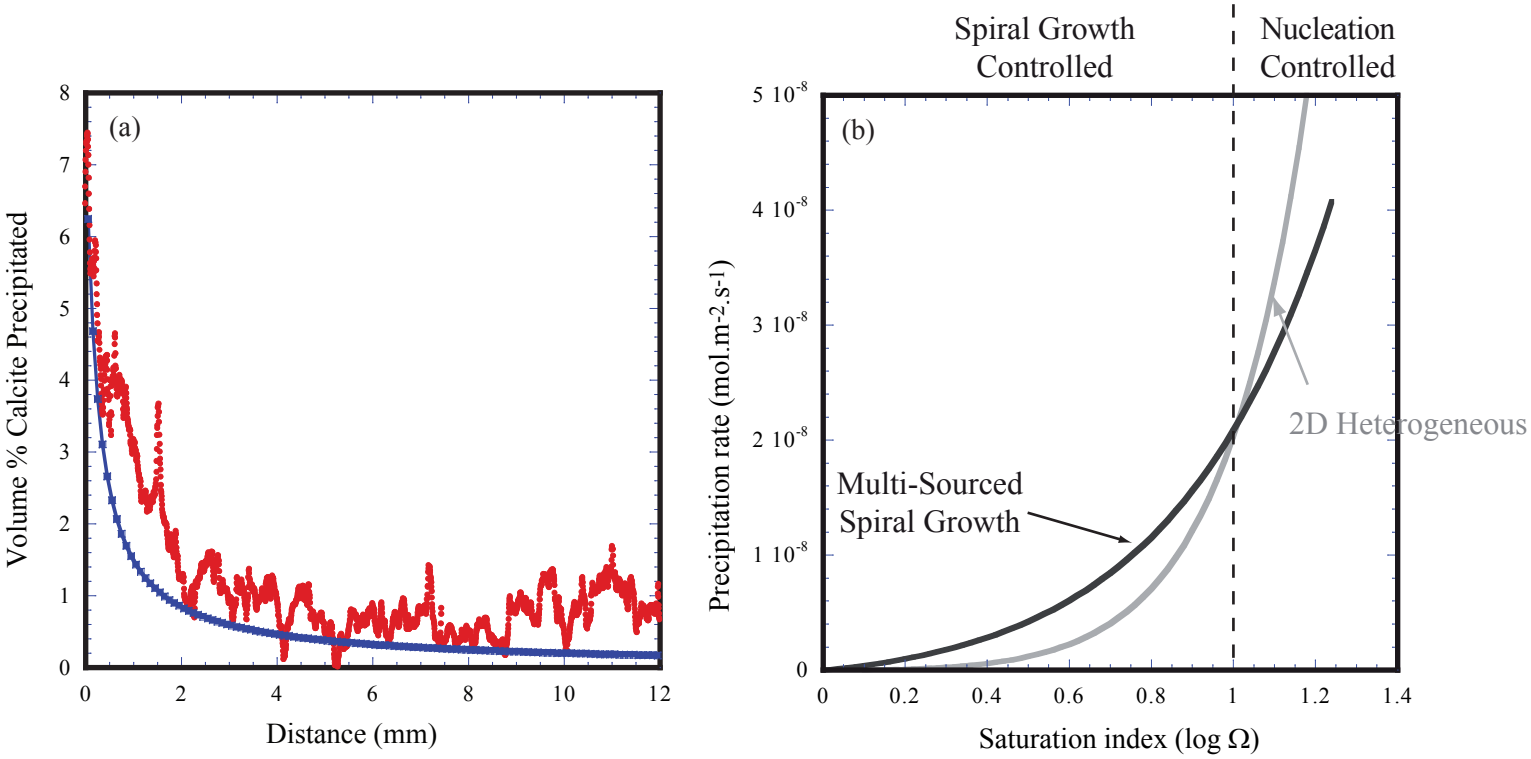

Figure 17. (a) Comparison of simulated profile of newly precipitated calcium carbonate with XMT data when two parallel rate laws are combined: 1) a partially diffusion controlled modification of the higher order rate expression suggested by Tang et al. [2008a] data, and 2) the nearly linear (n=1.12) multi-sourced spiral growth mechanism suggested by the stirred cell experiments in this study. The rates fromTang et al. [2008a], however, need to be slowed even beyond the modification imposed by a partial diffusion control in order to result in a reasonable match with the data. (b) Postulated precipitation rate regimes based on plug flow column experiments: spiral growth controlled (dark solid line) vs nucleation control (grey solid line).

DISCLAIMER

This document was prepared as an account of work sponsored by the United States Government. While this document is believed to contain correct information, neither the United States Government nor any agency thereof, nor The Regents of the University of California, nor any of their employees, makes any warranty, express or implied, or assumes any legal responsibility for the accuracy, completeness, or usefulness of any information, apparatus, product, or process disclosed, or represents that its use would not infringe privately owned rights. Reference herein to any specific commercial product, process, or service by its trade name, trademark, manufacturer, or otherwise, does not necessarily constitute or imply its endorsement, recommendation, or favoring by the United States Government or any agency thereof, or The Regents of the University of California. The views and opinions of authors expressed herein do not necessarily state or reflect those of the United States Government or any agency thereof or The Regents of the University of California.

Ernest Orlando Lawrence Berkeley National Laboratory is an equal opportunity employer.